Acta Materialia 202 (2021) 417–436

Contents lists available at ScienceDirect

Acta Materialia

journal homepage: www.elsevier.com/locate/actamat

Alloys-by-design: Application to new superalloys for additive manufacturing

Yuanbo T. Tang[a], Chinnapat Panwisawas[a], Joseph N. Ghoussoub[a], Yilun Gong[a], John W.G. Clark[b], André A.N. Németh[b], D. Graham McCartney[a], Roger C. Reed[a,c,*]

[a] Department of Materials, University of Oxford, Parks Road, Oxford, OX1 3PH, United Kingdom
[b] OxMet Technologies, Unit 15, Yarton, Kidlington, OX5 1QU, United Kingdom
[c] Department of Engineering Science, University of Oxford, Parks Road, Oxford, OX1 3PJ, United Kingdom

ARTICLE INFO

Article history:
Received 16 March 2020
Revised 7 September 2020
Accepted 7 September 2020
Available online 11 September 2020

Keywords:
Alloys-By-Design
Additive Manufacturing
Selective laser melting
Nickel-based superalloys
Cracking mechanisms
Micromechanics

ABSTRACT

New grades of γ/γ' nickel-based superalloy for the additive manufacturing process are designed using computational approaches. Account is taken of the need to avoid defect formation *via* solidification and solid-state cracking. Processing trials are carried out using powder-based selective laser melting, comparing with the heritage alloys IN939 and CM247LC. Microstructural characterisation, calorimetry and hot tensile testing are used to assess the approach employed. The superior processability and mechanical behaviour of the new alloys are demonstrated. Suggestions are made for refinements to the modelling approach.

1. Introduction

At present, nickel-based superalloys are used to make components either by investment casting, or else by machining to net shape from wrought feedstock [1]. Additive manufacturing (AM) offers the potential to alter this situation radically, to allow advantage to be taken of the greater precision, less scrappage and enhanced design freedom which this new process promises [2–4]. Indeed, there is reason to believe that this digital revolution is happening, as judged by the tremendous interest being shown in this technology worldwide [5]. For instance, additive manufacturing is being used with success to produce components in stainless steels [6,7], grades of titanium [8,9] and aluminium alloys [10].

Nevertheless, for the nickel-based superalloys, the application of AM has proved challenging [11,12]. Contributory factors are (i) their significant high temperature strength due to a high fraction of intermetallic phases and (ii) the wide freezing range arising from the extent of alloying needed to impart properties. Processing-related defects, in particular microcracks, are then promoted which can compromise mechanical behaviour [13–15]. Despite concerted efforts contributed worldwide, no consensus has been reached thus far on the dominant form of cracking [16–18]; more research is required to better understand the mechanisms of defect formation and the processing conditions which introduce and/or avoid them [2,19–21]. Furthermore, it is not clear whether existing alloys – which are used for investment casting for example – are best suited for this new process [22]. Probably, it will prove possible to design new grades of superalloy which can be processed in a superior manner to those currently available. After all, the existing heritage alloys were not designed with the AM process in mind. The research reported here was driven by this premise.

In this paper, computational modelling is used to isolate new grades of nickel-based superalloy specifically for additive manufacturing, using a design-driven methodology. So-called alloys-by-design (ABD) approaches are employed, to propose compositions which are predicted to display appropriate levels of strength and creep resistance, and which also possess adequate processability. Experimental trials *via* powder-based selective laser melting (SLM) were utilised to test our methods and in particular to propose a first generation alloy designated ABD-850AM. To verify the applicability of the ABD approach, two heritage alloys IN939 and CM247LC – spanning the alloy design space from medium to high γ' fraction and significant freezing range – were tested with the same processing parameters. The various cracking mechanisms were characterised and analysed. Rationalisation of the findings has allowed

* Corresponding author at: Department of Engineering Science, University of Oxford, Parks Road, Oxford, OX1 3PJ, United Kingdom.
E-mail address: roger.reed@eng.ox.ac.uk (R.C. Reed).

https://doi.org/10.1016/j.actamat.2020.09.023
1359-6454/

the composition of a further second-generation alloy, ABD-900AM, to be proposed, which contains a medium γ' fraction and demonstrably superior mechanical properties and printability.

2. Computational alloy design methodology

Computationally-intensive physics-based modelling has been used to design new grades of superalloy suitable for AM. Composition-dependent properties have been estimated for a very large number ($> 10^7$) of trial alloy compositions at 0.1 at% resolution, using sub-models linking chemical composition and properties/behaviour; the large datasets built up were then analysed to identify optimal alloys using, *inter alia*, Pareto front approaches and property estimates based upon design targets [23]. The sub-models used for yield strength, creep resistance and phase stabilities are those from proven efforts for both single crystal superalloys for investment casting [23,24] and powder-processed superalloys [25,26].

For additive manufacturing, the most important consideration is resistance to processing-related cracking, since the heat transfer characteristics of the process lead to very short heat source/powder interaction time and thus high rates of thermal straining [27]. This is the proven bottleneck of this digital technology [28]. Thus, for each trial composition in the dataset we made (in the first instance and inspired by the need for pragmatism) estimates of (i) the freezing range on the basis of a Scheil analysis of non-equilibrium solidification, assuming no back-diffusion; (ii) an estimate of the resistance to strain-age cracking during thermal cycling and post processing. In addition, in order to ensure the performance and stability of an alloy, estimates of (iii) yield stress and (iv) creep resistance, following the approaches of [25] and [23] respectively. This approach requires in turn estimates to be made of the anti-phase boundary energy, γ' fraction and interdiffusion coefficients. Finally (v) the susceptibility of the microstructure to topological close packed (TCP) phase formation was estimated by the energy level of d-block elements, following [23]. In the present work, much depends upon an accurate determination of the freezing range for different alloys, which is of course more-or-less experimentally inaccessible. We have discovered that the uncertainties in our calculated values depend upon three important factors namely: (i) the choice of thermodynamic database to use in the calculation; (ii) the list of phases included in the thermodynamic calculation for a given alloy; and (iii) the specific composition employed within the alloy's technical specification. It seems that the literature does not fully address these important points which are discussed further in the Appendix.

Fig. 1 illustrates the results of our calculations and informs the rationale for the choice of alloy compositions (labelled on all the sub-figures as ABD-850AM and ABD-900AM) made in this work. Fig. 1(a) illustrates a weldability diagram employed in our analysis, which has its origins in the welding community [27]. On it is located various existing alloys; difficult-to-process alloys are expected to lie towards the top right of the diagram and processable ones to the bottom left. The lines drawn correspond to limits for assumed bounds for risk of strain-age cracking, but such a diagram does not account for hot tearing resistance, for which the freezing range is important. Unsurprisingly, there is a strong correlation of strain age cracking merit index with γ' content and creep resistance (Fig. 1(b, c)), and also the implication that increased hardening by alloying of γ' by Ti, Nb and Ta demands a reduction in Al content; this implies the classical trade-off between manufacturability and materials performance. To account for hot tearing susceptibility, Fig. 1(d & e) illustrates the predicted trade-off between Scheil freezing range, phase constitution and anticipated strength. It is notable that the strength contour runs from bottom left to top right, which implies that alloys of higher strength typically possess larger γ' fraction and freezing range. A weak correlation in freezing range with γ' fraction was found, but note that – at any given γ' content – there is considerable scope for narrowing or widening the freezing range; this is due to the solidification path and the last stages of it, see Section 5.1. An upper limit for the freezing range of 280 K has been selected as a first approximation in this work, a value in between that for IN738LC (285 K) and IN718 (265 K). The former alloy has been reported frequently to suffer from hot cracking [29–31], but the latter has been found to be readily printable [32–34]. Likewise, the maximum strain-age cracking index is chosen as 4 wt% based on the micro-cracking reported in IN939 (4.3 wt%) [35]. Fig. 1(e) confirms that the new alloys ABD-850AM and ABD-900AM are close to the Pareto front for maximum predicted creep performance without excessive γ' fraction, in an attempt to limit the risk of strain-age cracking. Fig. 1(f) illustrates our design concept more generally – a minimum required creep strength at a maximum anticipated tolerable freezing range and strain-age cracking susceptibility.

In summary, one should note that our design analysis confirms that the chemical composition influences the predicted mechanical properties and processing behaviour in a complex non-linear manner, which could not have been anticipated without using the detailed modelling described here. Note also that we have not made use of blind empirical approaches based upon neural networks or machine learning, since there is a paucity of information on alloys for additive manufacturing in the literature. At this stage, we do not see how these could be successful.

3. Experimental methodology

3.1. Alloys for additive manufacturing

The majority of the work reported in this paper was conducted using the new alloy ABD-850AM, with CM247LC [11] & IN939 [35] – which are long-established superalloys spanning the alloy design space used widely for structural parts manufactured by conventional processes such as investment casting. In the latter part of the paper, results on a further alloy ABD-900AM are presented. Each alloy was obtained by argon gas atomisation, which produced a distribution of spherical particles with a D50 size of ~ 30 µm. The compositions of the powders, determined by inductively coupled plasma-optical emission spectroscopy (ICP-OES) and ICP-combustion analysis, are given in Table 1.

3.2. Processing parameters for selective laser melting (SLM)

To isolate the effect of alloy composition on defect formation, all alloys have been processed using an identical build strategy and set of laser parameters. The processing parameters used in the current study are the optimised parameters determined by Renishaw plc for CM247LC [36], and also provide suitable (but not necessarily optimised) processing parameters for IN939 & ABD-850AM. By way of background information, we have determined that the broad findings of our study presented here are not altered by modifications in the laser parameters employed [37].

A Renishaw AM-400 machine was employed, which uses a modulated 200 W ytterbium fibre laser to process powder feedstock within a 125 × 125 × 125 mm^3 build volume. The modulated laser performs point-to-point scans; the process parameters used were: laser power 200 W, layer thickness 30 µm, hatch spacing 50 µm, point distance 90 µm and exposure time at each point 50 µs. It possesses a reasonably small hatching distance, which promotes remelting that can heal some cracks [38]. A meander scan strategy – a raster scan with 67° rotation for each layer [39] – was used. For the processing trials, cubes of dimensions 10 × 10 × 10 mm^3 were manufactured for each alloy. Each layer scan of

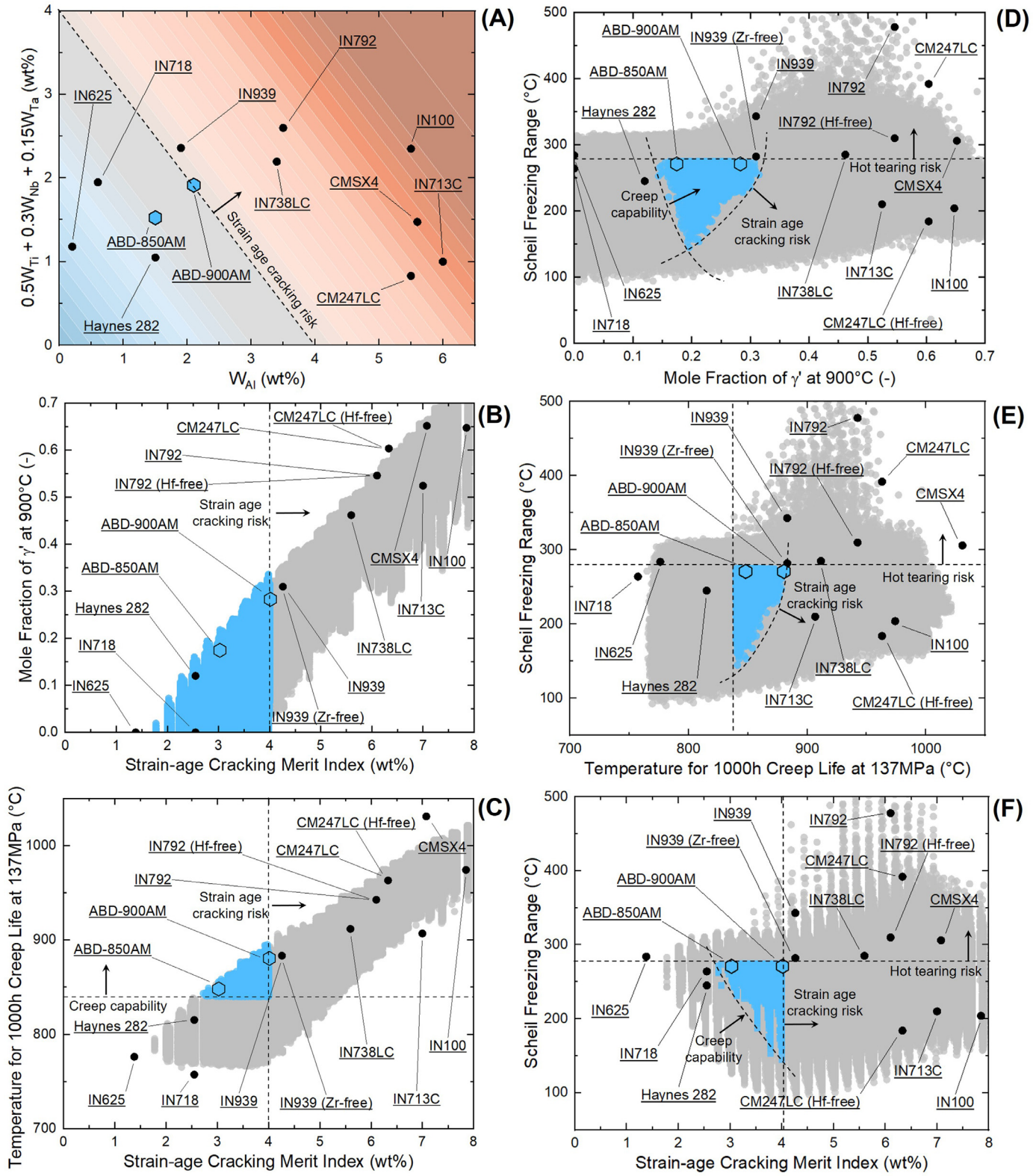

Fig. 1. Computational alloy design spaces used for new grades of superalloy; locations of heritage alloys are also plotted for comparison. (a) modified weldability diagram with maximum strain-age cracking index identified. (b & c) show strain-age cracking merit index and its relationship to γ' fraction and creep merit index. (d & e) presents magnitude of freezing range in relation to γ' fraction and creep merit index, where strain-age cracking and creep merit contours are indicated. (f) gives the final design space used to isolate new grades of alloy based upon freezing range, strain-age cracking index and minimum required strength & creep.

Table 1
Alloy composition for current study in wt-% (Ni-base), measured using ICP-OES, ICP-combustion (carbon) and Spark OES (boron).

	Ni	Cr	Co	Al	Ti	Nb	Ta	W	Mo	Hf	Zr	C	B
ABD-850AM	Bal	18.68	17.60	1.29	2.22	0.60	0.44	4.74	1.89	-	-	0.01	0.003
CM247LC	Bal	8.30	8.99	5.62	0.75	-	3.16	9.45	0.52	1.32	-	0.07	0.016
IN939	Bal	22.10	18.80	1.76	3.80	0.97	1.37	1.96	-	0.01	0.11	0.16	0.009
ABD-900AM	Bal	16.96	19.93	2.11	2.39	1.78	1.42	3.08	2.09	-	-	0.05	0.005

the SLM build was initially offset 100 μm from the edge of the 10 mm × 10 mm build cross-section. The region within the offset was scanned using the meander scan strategy. The offset border region was then scanned in two passes with the same power but at lower velocity (0.5 m/s) in order to improve the surface finish of the parts, consistent with industrial practice. The cube structure was built on top of 16 inverted pyramidal feet of the same material.

3.3. Quantification of the extent of cracking

The cracking behaviour was quantified using stereological assessment of a digitised optical micrographs. The transverse (XY-) plane, i.e. perpendicular to the building direction (Z), was sectioned at half height (Fig. 2a) and prepared using standard metallographic procedures involving polishing and finishing with a 40 nm colloidal silica suspension. The degree of cracking in each material were first captured in two locations, i.e. border and bulk, due to their large difference in cracking frequency found. The border region was designated by an area extending 300 μm from surface, and the rest is referred to here as the bulk. For each analysis, several random locations were captured and summed (~ 5 mm^2 in area) for analysis. The ImageJ software was then employed for image binarisation by applying a threshold to the histogram. Total cracking length over the area measured gives the metric of cracking density, in the unit of mm/mm^2, following the methods used in [11].

3.4. Electron microscopy: microstructure and micro-mechanical analysis

The microstructures were examined by a Zeiss Merlin field emission gun scanning electron microscope (FEG-SEM) on both transverse (XY-) and longitudinal (XZ-) sections of the SLM specimens, which are perpendicular and parallel to the build direction (Z) respectively. The XZ- and YZ-planes are assumed to be identical because of the meander scan strategy used. Since defect distribution has been a concern here, multiple backscattered electron (BSE) images of the XY-plane surface were obtained at 15 kV and stitched together. Samples were also electrolytically etched using 10% phosphoric acid at 3 V direct current. This etches away the γ matrix revealing γ' and carbide/boride particles. High resolution imaging of the microstructure following etching was undertaken using the secondary electron signal with the FEG-SEM, using immersion lens (in-lens/SE) and angle selective backscattered (AsB/BSE) detectors.

A Bruker electron backscattered diffraction (EBSD) system was used to investigate crystal orientation, texture and geometrically necessary dislocation (GND) distribution in the as-fabricated microstructures. To obtain inverse pole figure (IPF) and pole figure maps of the border and the bulk region, large area EBSD scans were conducted of samples both perpendicular and parallel to the build direction, with a step size of 1.12 μm. Grain size was measured using ESPRIT 2.1 software and is quoted as an equivalent grain diameter [40]. The pole figure contour is generated by HKL Channel 5 Mambo software [41].

To obtain information on GND distribution, high resolution EBSD (HR-EBSD) was conducted on the surfaces perpendicular to the build direction, both next to the border and within the bulk material. The patterns were stored at 400 × 300 resolution with a step size of 445 nm. A cross-correlation based method were used to process the stored EBSD patterns [42].

3.5. Assessment of mechanical behaviour

In the first instance, the Vickers microhardness of each alloy was measured in both the as-fabricated condition and also following a heat treatment schedule, details of which are in Table 2. The tests were carried out using a 0.3 kg force load applied for 10 seconds. Five tests were conducted in each material in the bulk region on both XY- and XZ-planes. Additionally, an electro-thermal-mechancial testing (ETMT) system was used for measuring the mechanical properties of the as-fabricated alloys at room temperature and at 800, 900 and 1000 °C. The samples were manufactured using identical conditions as for the cube samples, but now with a height of 52 mm. Uniaxial loading was applied in tension along the build direction for polished samples that were cut by electrical discharge machining (EDM). The sample geometry has a square cross-section of 1 mm length/width with a 16 mm parallel gauge. To minimise the effect from solid-state transformation kinetics during heating to the test temperature, in particular dynamic strain ageing, a heating rate of 100 K/s was employed and tests were performed at a strain rate of 10^{-2} s^{-1}. In the last part of the paper, all alloys were tested in fully heat treated conditions using ETMT, from ambient up to 1000 °C at a strain rate of 10^{-3} s^{-1}. The strain was measured using an iMetrum non-contact video extensometry method on a 3-mm gauge length where the temperature distribution is homogeneous. Full details of the experimental setup are described in greater detail in reference [43].

3.6. Differential scanning calorimetry (DSC)

Differential scanning calorimetry has proven useful for rationalising our findings, even though it is impossible to replicate with it the heating and cooling rates of the AM process. Melting and solidification behaviour (phase transformation temperatures) of the AM-processed microstructures was investigated using a Netzsch DSC 404 F1. Samples were cut using EDM into disks 3 mm in diameter and $\simeq$ 1 mm thickness. The measurements were carried out in a flowing argon atmosphere (20 ml/min). The differential heat flux was recorded at a heating rate of 10 K/min to 1450 °C, held for 15 mins and then cooled at the same rate. Baseline calibration runs were performed with an empty crucible and temperatures were calibrated in separate experiments using standard reference material.

4. Results

4.1. Overview of defect formation: cracking, porosity and lack of fusion

Fig. 2 (b–d) illustrates the entire cross-sections built for each alloy in the XY-plane (perpendicular to the build direction) in the

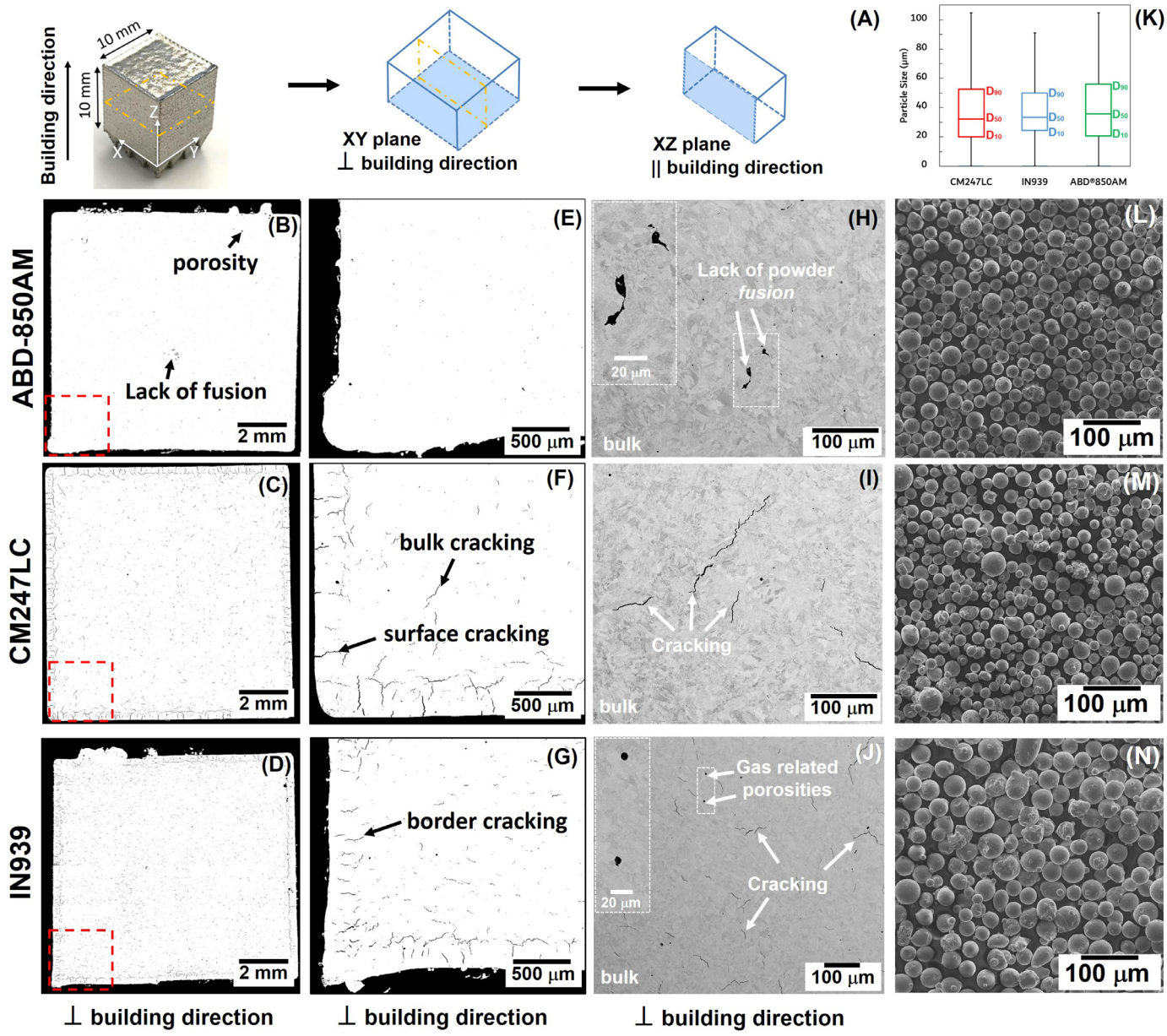

Fig. 2. Overview of as-fabricated microstructures of ABD-850AM, CM247LC and IN939, viewed perpendicular to the build direction. (a) shows the XY- and XZ-planes sectioned for each cube. (b–d) illustrates the stitched cross-sectional area of the XY-plane using digitised SEM images and (e–g) are magnified corners of these. (h–j) demonstrates typical lack of powder fusion, cracking and gas-related porosity. (k) shows the powder size distribution which is taken from the powder in (l–n).

Table 2
Heat treatment program conducted for the alloys.

	Solution	Cooling	Stablisation	Cooling	Ageing	Cooling
ABD-850AM	980 °C/2h	Air	850 °C/4h	Air	760 °C/16h	Air
CM247LC [11]	1260 °C/2h	Air	1079 °C/2h	Air	871 °C/20h	Air
IN939 [69]	1160 °C/2h	Air	1000 °C/4h	Air	850 °C/16h	Air
ABD-900AM	1050 °C/2h	Air	850 °C/4h	Air	760 °C/16h	Air
IN718 [70]	980 °C/2h	Air	720 °C/8h	Furnace	620 °C/8h	Air

as-fabricated state. Each is a montage stitched together from 24 binarised SEM images to better reveal the defect shape and locations. Cracking is heavily pronounced in both legacy alloys CM247LC and IN939; some cracks can extend over 300 μm and are visible to the naked eye, e.g. Fig. 2(e), (f) & (h). Furthermore, the frequency of cracks in the border scan regions are significantly higher than the bulk. However, at the resolution of the imaging conditions employed, no cracks were observed in the newly designed alloy ABD-850AM.

Crack density in both border and bulk locations has been estimated in the legacy alloys: 6.7 & 0.8 mm/mm^2 in CM247LC and 5.0 & 1.6 mm/mm^2 in IN939, respectively. Surface connected cracks – which cannot be healed by hot isostatic pressing (HIP) – have also been examined, and are 35 times more frequent in CM247LC than

Table 3
Powder size distribution in μm of the three alloys studied.

	Min	D10	D50	D90	Max
ABD-850AM	0.1	20.6	35.8	56.1	104.7
CM247LC	0.1	19.9	32.3	52.7	104.7
IN939	0.1	24.4	33.5	50	91.2

in IN939. Other defects such as spherical gas porosity and lack of powder fusion, which occur less frequently, were also noted, see Fig. 2(i) & (j). The former is observed in all the alloys and occasionally in association with cracks. Pores occurred more frequently close to the border regions than in the bulk. Lack of powder-fusion defects occur infrequently in all alloys. Due to their low occurrence and/or small size these two types of defect have not been examined further in this work.

For the avoidance of doubt, the size and morphology of the starting powder was checked for consistency. The powder size distributions are very similar, as determined by laser diffractometry, see Fig. 2(k). The D10, D50 (median) and D90 values are given in Table 3. All three powders were found to exhibit a near-spherical external morphology with only a few satellite particles, see Fig. 2(l–n). The inescapable conclusion is that it is the alloy composition which is influencing processability.

4.2. Detailed characterisation of cracking modes

In what follows, the cracking behaviour is characterised carefully. Although it is not ideal, we make use of the phenomenological classification described extensively in the welding literature [44–46]. We have categorised the observed bulk cracking into three types based upon detailed fractography characterisation: (i) solidification cracking (which is related to the hot tearing phenomenon), (ii) liquation cracking, and (iii) solid-state cracking. The comparison of border and bulk cracking will be discussed in detail in Section 4.5. The following section emphasises CM247LC and IN939, which display extensive cracking.

Fig. 3, taken from the XZ-plane, displays locations in CM247LC and IN939 that indicate solidification cracking has occurred. The rounded features of cells and dendrite arms are evident which confirms separation occurred whilst a remnant of liquid was still present and that there was insufficient feeding of remaining liquid to accommodate the solidification shrinkage strain in this region. Moreover, nano-metre sized MC type carbides are also visible within the intercellular regions, which would have formed during solidification and which would also act to inhibit feeding. This type of cracking normally leaves a large gap between the two surfaces with an irregular shape, where the two surfaces do not necessarily appear in the same morphology that can close up together. Because of this feature, solidification cracks are the easiest to identify.

Evidence of liquation cracking has also been observed, see Fig. 4, but only in CM247LC. There was no definitive observation of this feature in either IN939 or ABD-850AM.

Fig. 4 (a–c), from the XY-plane, confirms cracking along a grain boundary using secondary electron (SE) and backscattered electron images. The BSE image (Fig. 4(b)) shows fine spherical MC-type carbides distributed in interdendritic regions. The higher magnification SEM image, see Fig. 4(c), shows γ/γ' eutectic phases are also present which is consistent with liquated regions, and observations of them reported in the literature [14]. Fig. 4(d) & (e) illustrate a crack and its adjacent phases after etching. The grain boundary phases close to carbides exhibit an alternating lamellar morphology, confirming a γ/γ' eutectic region. Furthermore, fine particles are also observed within the matrix near the eutectic in Fig. 4(f), which is likely to be γ'. Fig. 4(g-i) illustrates another example of liquation from the XZ-plane. The melt pools are outlined in (g) and clearly show the initiation is in the vicinity of melt pool heat affected zone (HAZ). Additionally, the crack tip in (h) again shows segregation of heavy element (i.e. high atomic number) where a liquid film is observed (i).

The precipitates are only observed near the bottom of the build in CM247LC, and it is increasing difficult to find them in other locations. Their size (see Fig. 4(f)) is estimated to be ~ 20 nm, which is in accordance with TEM results in the literature [12]. The formation of precipitation is believed to be triggered by the heat treatment inherent to the SLM process, whereby each point in the AM build is re-heated multiple times as the laser passes the vicinity of the region.

In contrast to the above cracking modes which clearly involve both solid and liquid phases, a further category is associated with cracking entirely in the solid state; it will be referred to here as solid-state cracking. This type of cracking can be clearly differentiated by careful metallographic analysis, as it possesses none of the aforementioned characteristics, i.e. exposed dendrites and/or traces of liquid films. The surfaces on each side are almost identical to each other in shape, typically microscopically “clean”, straight and often associate with sharp kinks. It is often also referred to as ductility dip cracking (DDC) and/or strain-age cracking (SAC) [46–48]. Evidence for this type of cracking is shown in Fig. 5 for both CM247LC and IN939. In the XZ-plane, solid-state cracking follows grain boundaries whilst exhibiting kinks which can be as sharp as 90° and in some instances interacting with solidification cracks. Typical crack lengths exceed 100 μm; sometimes they can extend over 300 μm, which is significantly larger than the melt pool size (around 60 μm). For avoidance of doubt, long cracks are not necessarily generated in the solid-state, but could result from the propagation of cracks that nucleated as hot tears.

Electrolytic etching was applied to IN939 to better illustrate the relationship between the melt pool and crack path (Fig. 5(d–f)) and it is clear that cracks cut through several layers of melt pool without the presence of exposed dendrites, further suggesting its differences to hot tears. Based on these observations – with no evidence of liquated phases at the grain boundaries and their straight clean character – a solid-state mechanism is responsible. Further validation of this mechanism through high temperature tensile tests will be discussed in Section 5.2.

4.3. Location dependency on microstructure and texture development

Fig. 6 (a–c) displays inverse pole figure (IPF) maps both parallel and perpendicular to the building direction (Z). These were derived from large-area EBSD scans (covering an area of 0.98 mm^2) performed in the bulk of each alloy. For all three alloys, the IPF maps reveal a strong texture dominated by preferential alignment of columnar grains along the building direction. However, the grains in ABD-850AM and IN939 are less elongated.

The microstructures of the as-fabricated alloys as revealed by etching are given in Fig. 6(d–f). Evidence is the epitaxial growth from partially remelted previous layers that allows the strong texture to develop. Microstructures perpendicular to build direction confirm the growth front to be predominantly cellular – cell sizes for each alloy vary between 300 nm to 1.5 μm, depending on the location. The spacing between primary cells is indicative of extremely high solidificaton rates. In CM247LC, the cell boundaries also exhibit γ/γ' eutectic mixture as expected in this alloy from the DSC results presented later and as previously observed elsewhere [14].

The contour pole figures plots quantify the texture strength for the three plane families {1 0 0} {1 1 0} and {1 1 1} with respect to the XY-plane of the sample. They confirm that the {1 0 0} texture component is the strongest among the three, and it is parallel to the building direction. It is notable that the texture strength is also

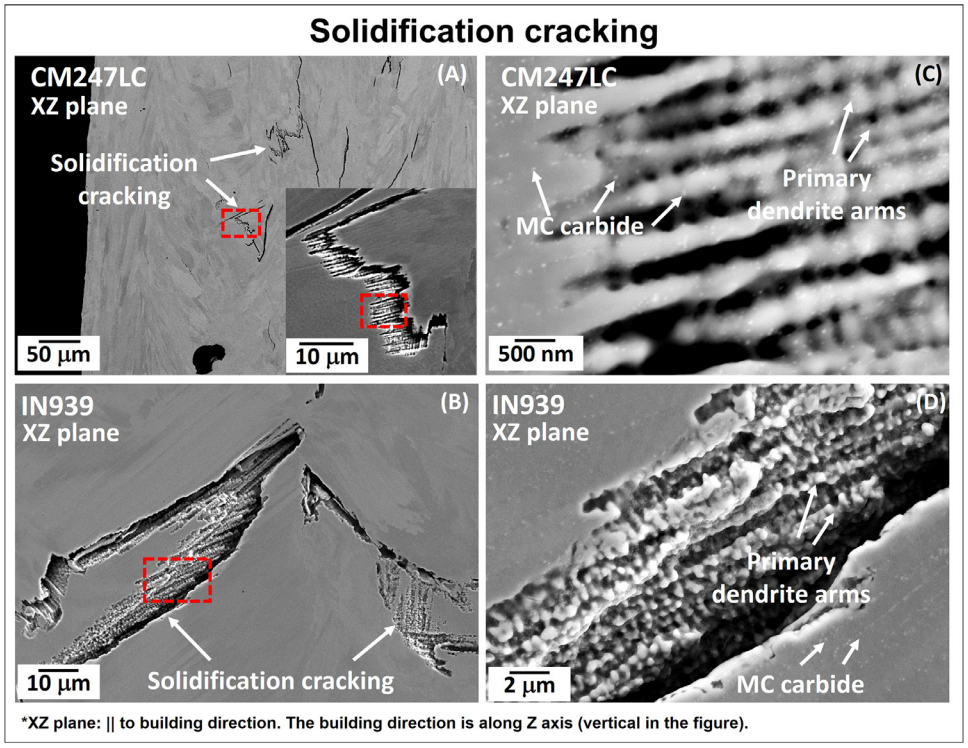

Fig. 3. Solidification type cracking observed in both CM247LC and IN939 in the XZ-plane of the as-fabricated microstructure. The primary dendrite arms are evident as they were separated during the last stages of solidification. The building direction is along the Z-axis.

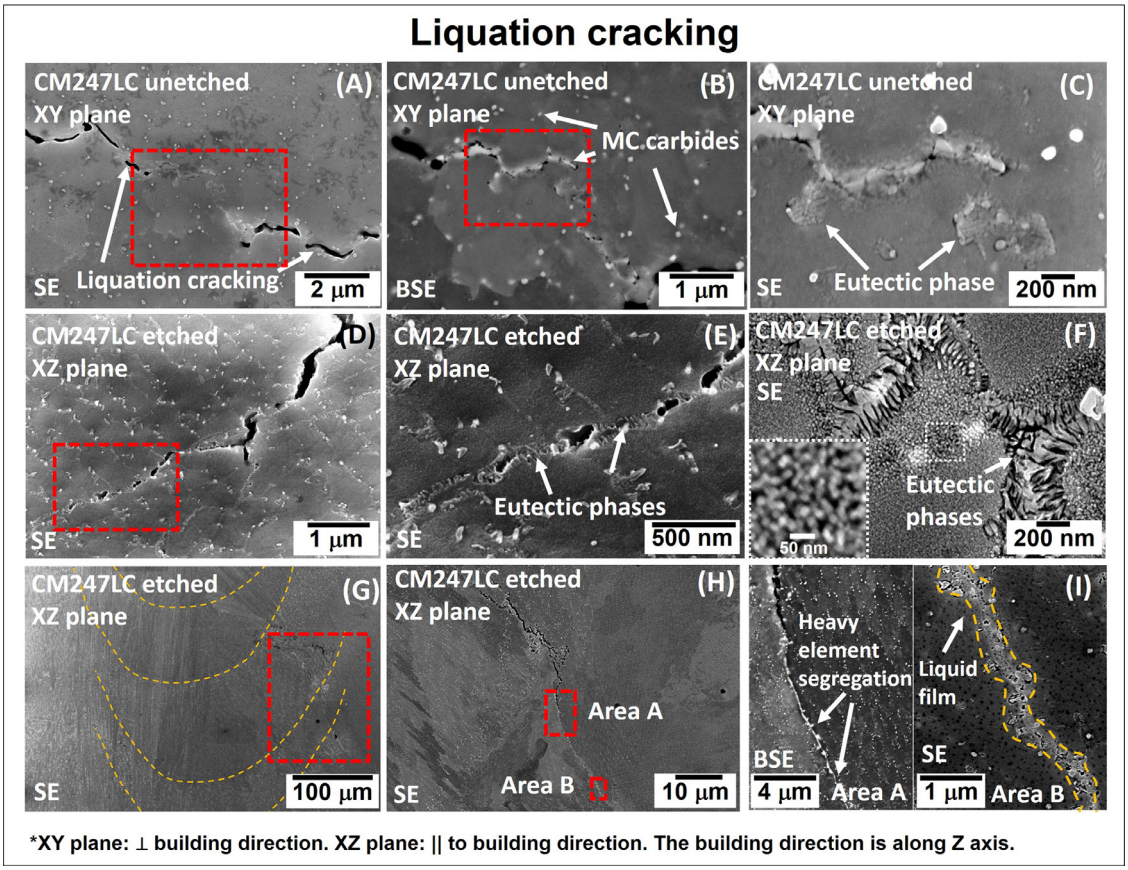

Fig. 4. Liquation type cracking in CM247LC as identified without etching (a–c) and with etching (d & e) in the as-fabricated microstructure. Area in red boxes are shown in more detail. Crack tip characterisation shows MC type carbide and γ/γ' eutectic phases are present along cracking. Nanometre size γ' particles are also visible with etching (f). A further liquation cracking site showing segregation and liquid film in (g-i). The building direction is along the Z-axis.

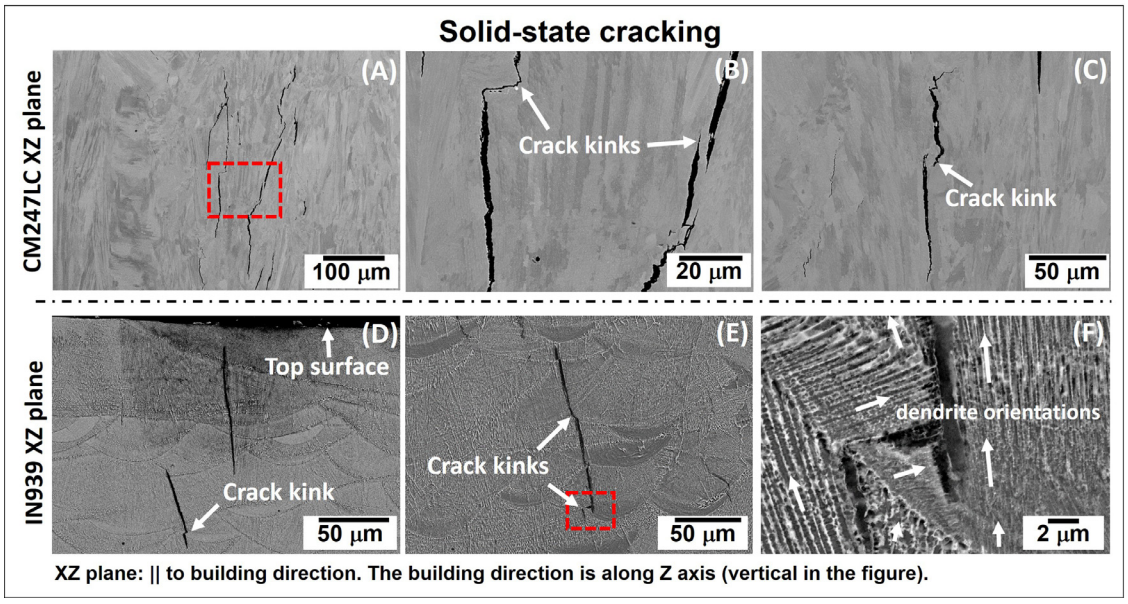

Fig. 5. Solid-state cracks observed in CM247LC (a–c) and IN939 (d–f) on XZ-plane in the as-fabricated microstructure. The cracking features no solidifying dendrites or liquation regions. Cracks normally exceeds 100 μm in length that propagate through several layers of melt pool. Area in red boxes are shown in more detail. The building direction is along the Z-axis.

alloy dependent due to their intrinsic thermophysical properties — CM247LC and IN939 have similar texture strength whilst the ABD-850AM {1 0 0} texture strength has been found to be considerably weaker.

Since there are significant differences of cracking susceptibility at different locations, the texture development from surface to bulk was studied. Fig. 7 shows IPF maps obtained from large-area EBSD scans from the border to the bulk in all three alloys for the XY- and XZ-planes in the as-fabricated condition. Clear differences in grain structure development are evident. Three regions are clearly distinguishable, as indicated using dotted lines: (i) small grains at the border; (ii) columnar grains at the border, and (iii) elongated textured grains in the bulk. To probe the change in the microstructure with respect to location, each EBSD map was segmented into ten equal width rectangular areas to estimate texture and grain size – their variation with distance from the border are shown in Fig. 7(g-i). Grain size and texture variations are broadly similar from alloy to alloy. In the border, small grains are around 20 μm and a local maximum is reached by columnar grains at around 80 μm. In the bulk region, grain size and texture remains relatively uniform. The texture component follows a similar trend to grain size.

Grain misorientation in the vicinity of cracks was investigated with EBSD. Based on 200 observations, cracks occur at high angle grain boundary (HAGB) regardless to their locations – both border and bulk. In addition, all HAGB cracking was found to be associated with solid-state and/or solidification reactions.

4.4. Spatial heterogeneity in GND distribution

As confirmed by Figs. 2 and 7, border and bulk regions displayed significantly different microstructures, which potentially influences the cracking phenomenon. This cannot be ignored because near surface cracking at the border cannot be healed by hot isostatic pressing (HIP), and hence it determines the quality of net shape finish and manufacturing precision. In the current study, smooth surfaces were achieved in contrast to components without [49] using the border parameter described in Section 2.2. However, the border scan also promotes local grain growth and cracking.

ABD-850AM has been studied by HR-EBSD in detail to determine its micromechanical response – since no cracks were observed, the stress/strain relaxation induced by cracking cannot then arise. The GND density and IPF maps are shown in Fig. 8. A distinctive bimodal distribution of GND density was observed in the AM process, which is very different from the usual single modal distribution with uniaxial deformation [50]. It suggests that some grains possess higher GND density than the others as a result of SLM fabrication. The high and low GND regions can even be present in the same grain, as labelled. A possible cause may be the preferential fibre texture in the building direction of [0 0 1]. The grains can allow large thermal expansion along [0 0 1], the build direction, due to the anisotropy developed, but constrained laterally in plane.

The bimodal GND distribution shown in Fig. 8(c) & (f) confirms a clear difference between the two different locations. Each histogram constitutes with two peaks where $log_{10}(\rho)$ equals 14.1 and 14.9. The microstructure on the border exhibits a higher population of GND associated with the latter peak compared to the bulk, which implies more plasticity involved. This is expected from the macroscopic stress state expected at the border, since tensile forces will be induced there. Furthermore, the effect may also be amplified due to the larger grain size as strain accommodation is then harder. Admittedly, the higher GND distribution on the border provides more mechanical driving force to facilitate cracking, making it more vulnerable than the bulk. As a result, in the legacy alloys for which cracking occurs, higher cracking densities near the border is frequently observed.

4.5. Characteristics of phase transformations during melting and solidification

The DSC thermograms acquired during the heating cycles of the three different alloys are shown in Fig. 9. The heating curves reflect the non-equilibrium microstructure in the as-fabricated state and the values of the transformation temperatures measured are listed in Table 4. In all three alloys, an abrupt change in heat flow is observed at the γ' dissolution temperature. But this feature is only just detectable in the ABD-850AM alloy whereas in CM247LC the onset of melting appears to overlap with the dissolution of γ'

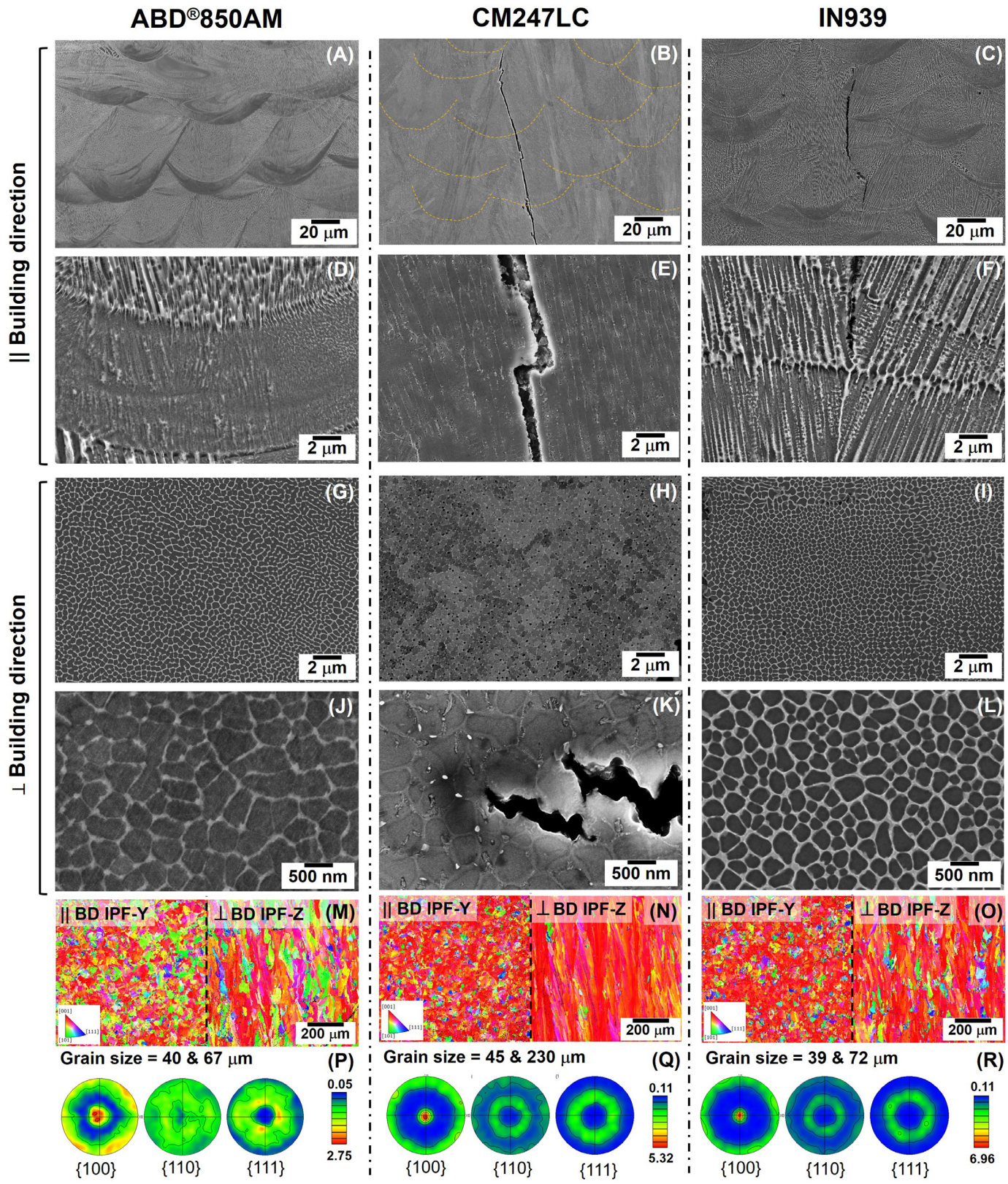

Fig. 6. SEM (etched), IPF and pole figure maps of the three alloys representing preferred texture in the bulk of materials (as-fabricated). (a–f) microstructure of XZ-plane in two magnifications and (g–l) microstructure of XY-plane in two magnifications. (m–o) illustrates the IPF of both planes along building direction and (p–r) demonstrates the bulk texture strength of {1 0 0}, {1 1 0} and {1 1 1} poles.

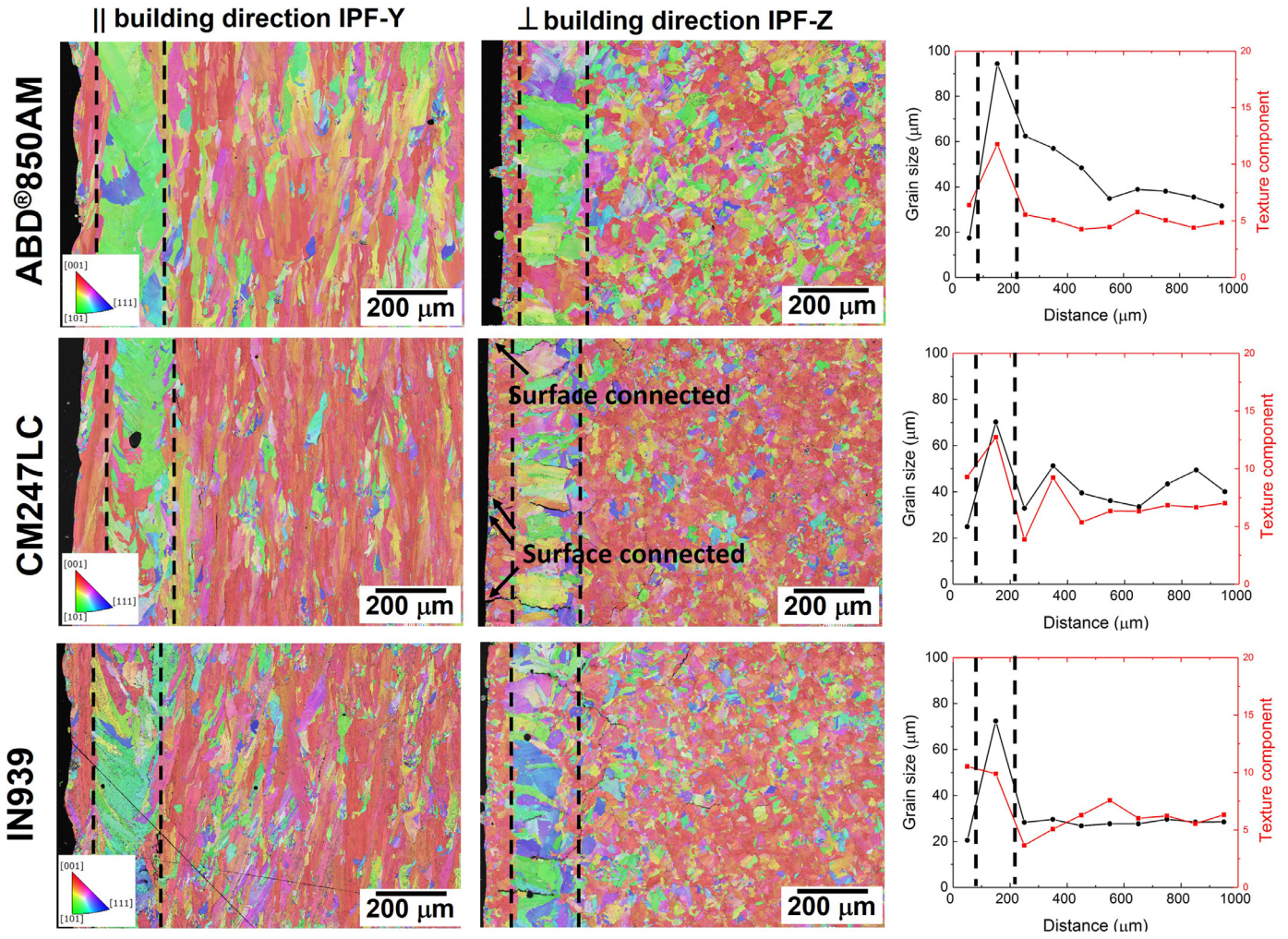

Fig. 7. EBSD scans near the border in orientations both parallel (XZ-) and perpendicular (XY-) to the building direction in the as-fabricated microstructure. Three regions of distinctive crystal orientations were indicated using dotted lines, where the grain size and {1 0 0} texture component profile vary across the distance.

Table 4
Phase transition temperatures in the alloys measured using DSC.

	DSC (10 K/min)					
	Heating (°C)			Cooling (°C)		
	CM247LC	IN939	ABD-850AM	CM247LC	IN939	ABD-850AM
γ'	1250	1088	1025	1181	1072	1013
T_S (Solidus)	1260	1206	1330	N/A	N/A	N/A
MC carbide	1360	1319	1353	1320	1295	1296
T_L (Liquidus)	1375	1330	1383	1372	1327	1377

as also noted elsewhere [12]. On heating, the temperatures corresponding to the onset of melting (T_S) and end of melting (T_L) were obtained by the extrapolation method [51]. Of particular note is the very sharp onset of melting of ABD-850AM at ~ 1383 °C. In CM247LC and ABD-850AM, there is a noticeable change in heat flow prior to melting, presumably due to dissolution of the carbide phase. But in IN939 the carbide/boride dissolution cannot easily be de-convoluted from matrix melting. Also shown in Fig. 9 are the thermograms resulting from slow cooling and solidification in the DSC. Values for T_L, carbide/boride formation, end of solidification and γ' formation are given in Table 4. In all three alloys the value of T_L on cooling is significantly lower than on heating, mainly due to nucleation undercooling. In CM247LC, there is a clear eutectic reaction at 1260 °C, T_E – probably involving γ, γ' and carbide – which is absent in the other two alloys.

4.6. Hardness response in the as-fabricated microstructures

Clearly, the mechanical response of the as-printed alloys is critical to determining whether solid-state cracking occurs. As a first test of whether this effect is relevant, microhardness tests have been carried out in the as-fabricated state, see Fig. 10(a). The error bars represent the standard deviation in the measurements. In the as-fabricated condition, ABD-850AM has the lowest Hv value whereas the two legacy alloys are notably stronger. This effect arises because ABD-850AM contains little if any γ' precipitation in the as-fabricated state, see Fig. 4(d–f), so that contribution to strengthening must be due to solid-solution hardening and/or substructural hardening. Clearly, the kinetics of γ' precipitation are sluggish in ABD850AM, which may be a contributory factor to its superior processability; this is explored in greater detail later. In-

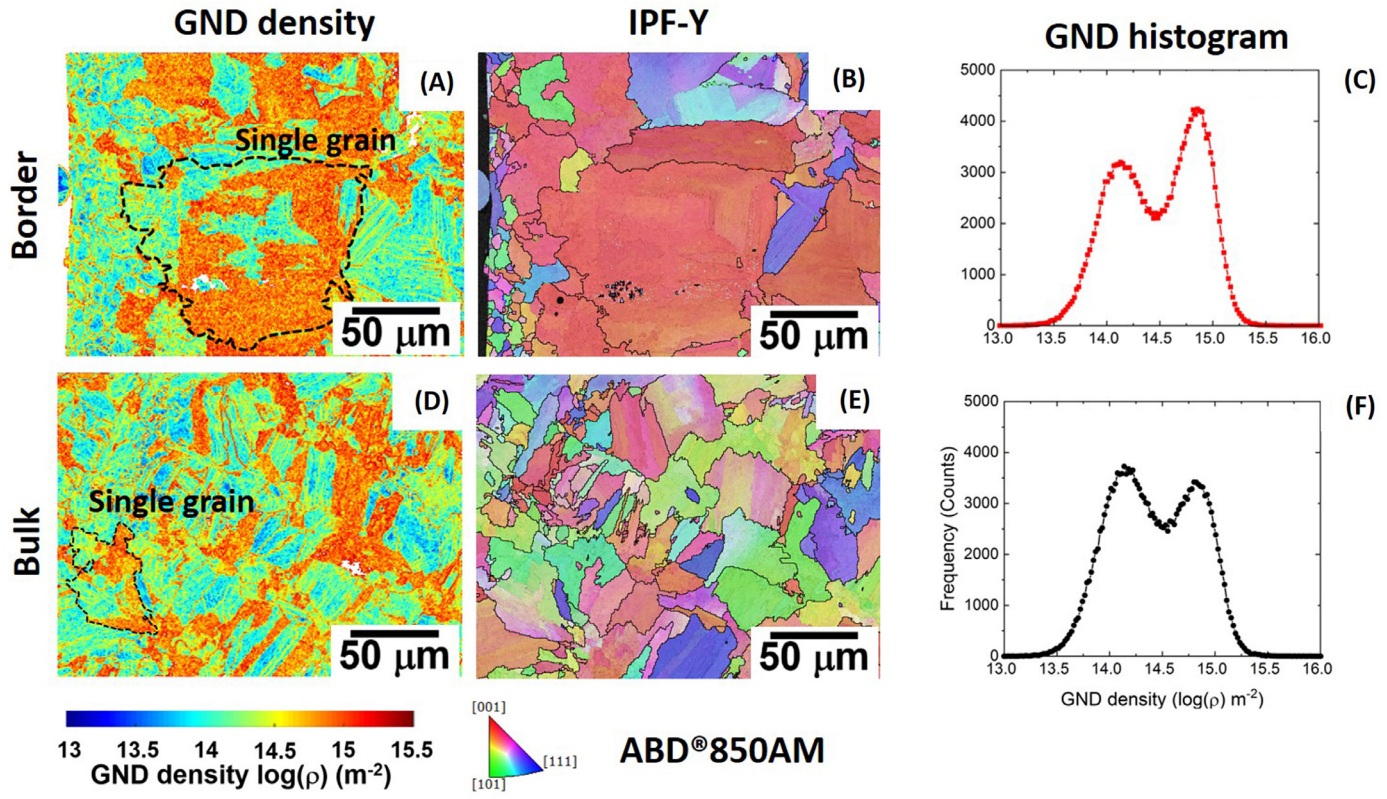

Fig. 8. GND density, IPF (Y-axis) and GND histogram maps are presented in the border and the bulk part of ABD-850AM in the as-fabricated microstructure. Local GND heterogeneity is observed, the histogram reveals a bimodal distribution.

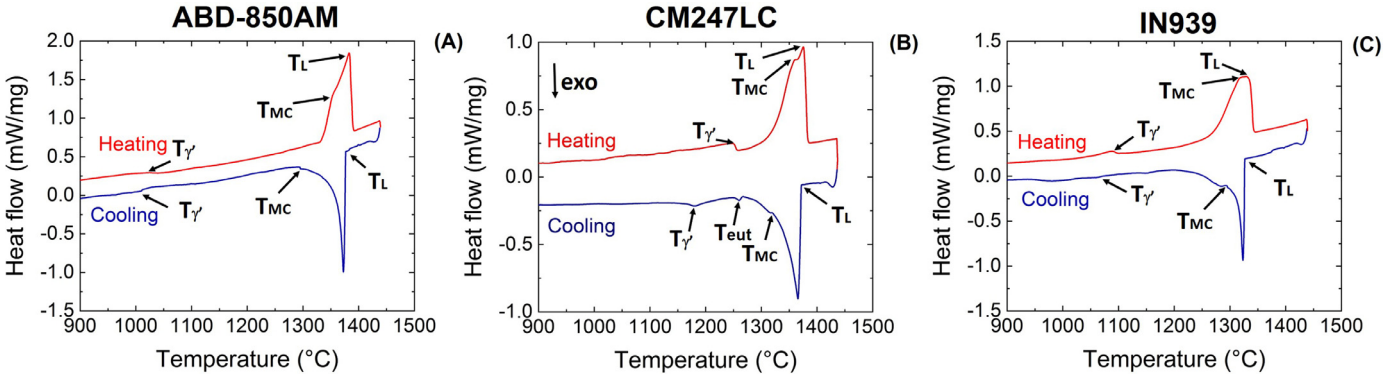

Fig. 9. Differential scanning calorimetry (DSC) curves obtained from the three alloys during heating and cooling at 10 K/min (a–c). Notable phase transformation temperatures are shown by the arrows and values are given in Table 4.

terestingly, with appropriate heat treatment, all alloys developed precipitation of γ', and also some γ'' in IN939, see Fig. 10(b-d). This allows both ABD-850AM and IN939 to harden significantly – by ~ 140 Hv and 90 Hv respectively – in contrast to only a small increase for CM247LC of ~ 10 Hv. Moreover, an orientation effect is evident with differences between the hardness on the XY-and XZ-planes. This trend is unchanged following heat treatment.

5. Discussion

By carefully controlled processing and characterisation studies, this work has demonstrated clearly the significant impact of alloy chemistry on susceptibility to defect formation (Table 5), microstructure development and hardness response by heat treatment. In particular, it has proved that theory-based modelling approaches are likely to prove fruitful for designing new grades of alloy for the new AM technology. Nevertheless, the results presented thus far require rationalisation, and moreover they provoke many further questions which demand attention.

5.1. Solidification at final stage: criteria and key elements

Although the high solidification cracking susceptibility of CM247LC and IN939 can be rationalised on the basis of their wide freezing ranges, the analysis thus far has limitations since it fails to take account of the very last stages of the solidification path which are acknowledged to be very important and potentially decisive [19,31]. Thus we now employ a more detailed analysis as proposed by Kou [52], who adapted the model of Rappaz et al. [53,54], to rationalise the resistance to hot tearing in the vulnerable regime. The critical feature emphasised is the balance between the strain rate of the solidifying solid (promoting cracking) and the

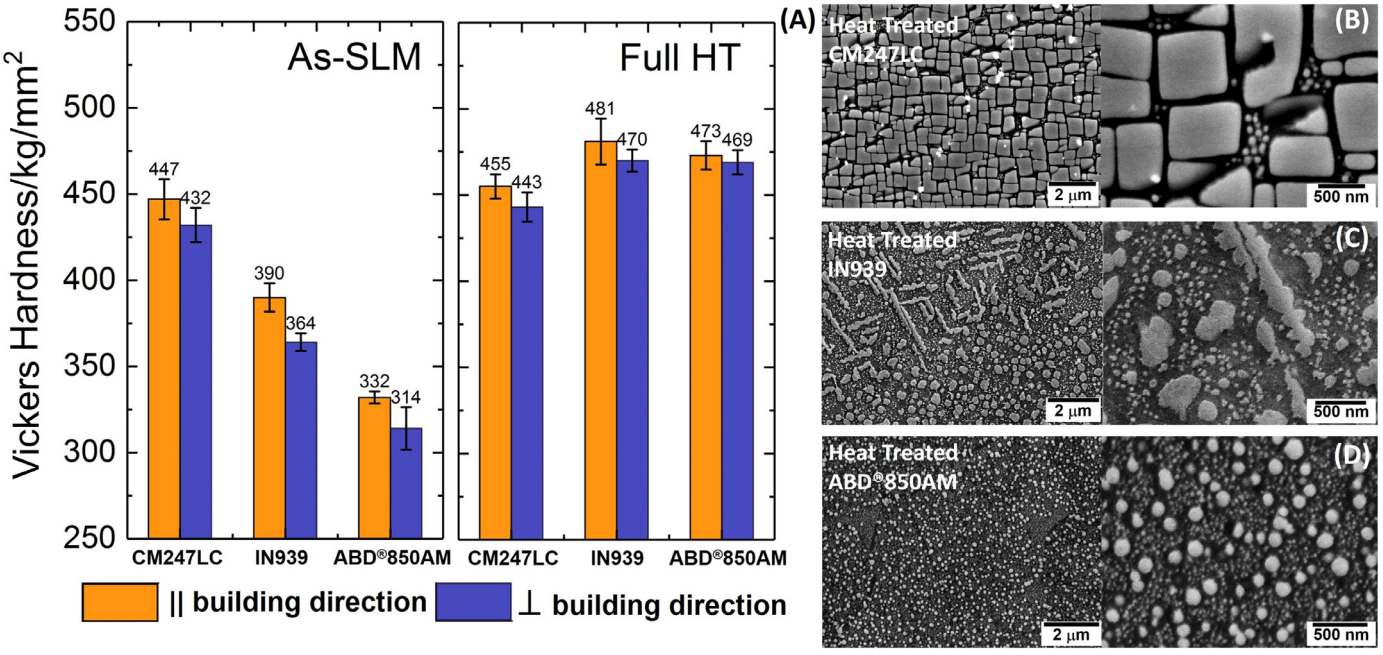

Fig. 10. (a) Vickers hardness, Hv, for as-fabricated and fully heat-treated microstructure parallel and perpendicular to the building direction, (b–d) etched microstructure of CM247LC, IN939 and ABD-850AM at two magnifications.

Table 5
Summary of defect formation in the three alloys.

	Cracking			Porosity	Lack of fusion
	Solidification	Liquation	Solid state		
ABD-850AM	N	N	N	Y	Y
CM247LC	Y	Y	Y	Y	Y
IN939	Y	N	Y	Y	Y

feeding rate of liquid (inhibiting cracking). The solidification cracking index (SCI) is then given by Kou [52]

$$\mathrm{SCI} = \left| \mathrm{d}T/\mathrm{d}(f_s^{1/2}) \right| \quad (1)$$

where f_s is solid fraction, T is temperature. It has been clarified by Kou [52] that the use of one specific temperature interval, for example $0.87 < f_s < 0.94$ originally proposed [52], is somewhat arbitrary. Hence we present the SCI values over the whole range of f_s, and then select three ranges at the last stage to discuss the cracking susceptibility over the three alloys, in addition, another two commonly studied alloys IN738LC and IN718, as well as two variants of IN939 and CM247LC, were analysed.

The SCI plots of f_s versus $|\mathrm{d}T/\mathrm{d}(f_s^{1/2})|$ are displayed in Fig. 11(a) over the range $0 < f_s < 0.99$ and (b) $0.8 < f_s < 0.99$. One sees that the cracking index increases drastically in the later stage, when $f_s > 0.8$. The magnified graph in Fig. 11(b) exemplifies the propensity for each material to undergo solidification cracking. The discontinuities in curves correspond to phase transformations. The average SCI values are evaluated over critical f_s ranges of 0.8–0.9, 0.9–0.99 & 0.8–0.99, see Table 6. The SCI values are reasonably similar for the three alloys in the range of 0.8–0.9, but the variation becomes significant in the other two f_s ranges. The key difference is likely to be $0.9 < f_s < 0.99$, which is crucial for AM superalloys.

The same analysis was also conducted for IN718, IN738LC and ABD-900AM, see Fig. 11(c). The former two heritage alloys have been frequently investigated in the AM field, where IN718 is deemed to be printable and whilst IN738LC is not. It is clear that for $f_s > 0.85$ IN718 exhibits rather low SCI values, whereas IN738LC possesses notably higher values. The average SCI of IN718 over the critical range $0.9 < f_s < 0.99$ is substantially less than that of IN738LC, consistent with their drastic differences in processability. It is interesting to note that although both alloys possess similar freezing range, the last stages of solidification are predicted to be very different due to their profoundly different alloying strategy. In case of doubt, ABD-900AM will be thoroughly discussed in Section 6. Consequently, the SCI analysis of these alloys supports the experimental observations that CM247LC is undoubtedly more prone than the other alloys. Other difficult-to-process alloys, IN939 and IN738LC, also have SCI values significantly higher than the AM suitable alloys, such as ABD-850AM and IN718.

Moreover, it is also worth pointing out that recent literature emphasises the significance of Hf and Zr [31,55] in affecting susceptibility to cracking; the SCI index also helps to rationalise their roles. Consistent with their partitioning characteristics, they are enriched in the vulnerable regime of the last liquid to solidify. Sensitivity tests for removing both elements were carried out by Scheil analysis whilst keeping other procedures unchanged, the new variants are named CM247LC Hf free and IN939 Zr free. The SCI values at the critical range $0.9 < f_s < 0.99$ (see Table 6) for those alloys are markedly reduced which suggests improved resistance to hot cracking, as experimentally validated elsewhere [55]. Nevertheless, a compromise in the mechanical performance due to the removal of these grain boundary strengtheners is expected [56,57].

In summary, the SCI analysis further helps to rationalise the results, yet it is not without some limitations. For example, the possible interactions between solidified phases and the last liquid are ignored – borides or carbides can serve as physical obstacles to re-

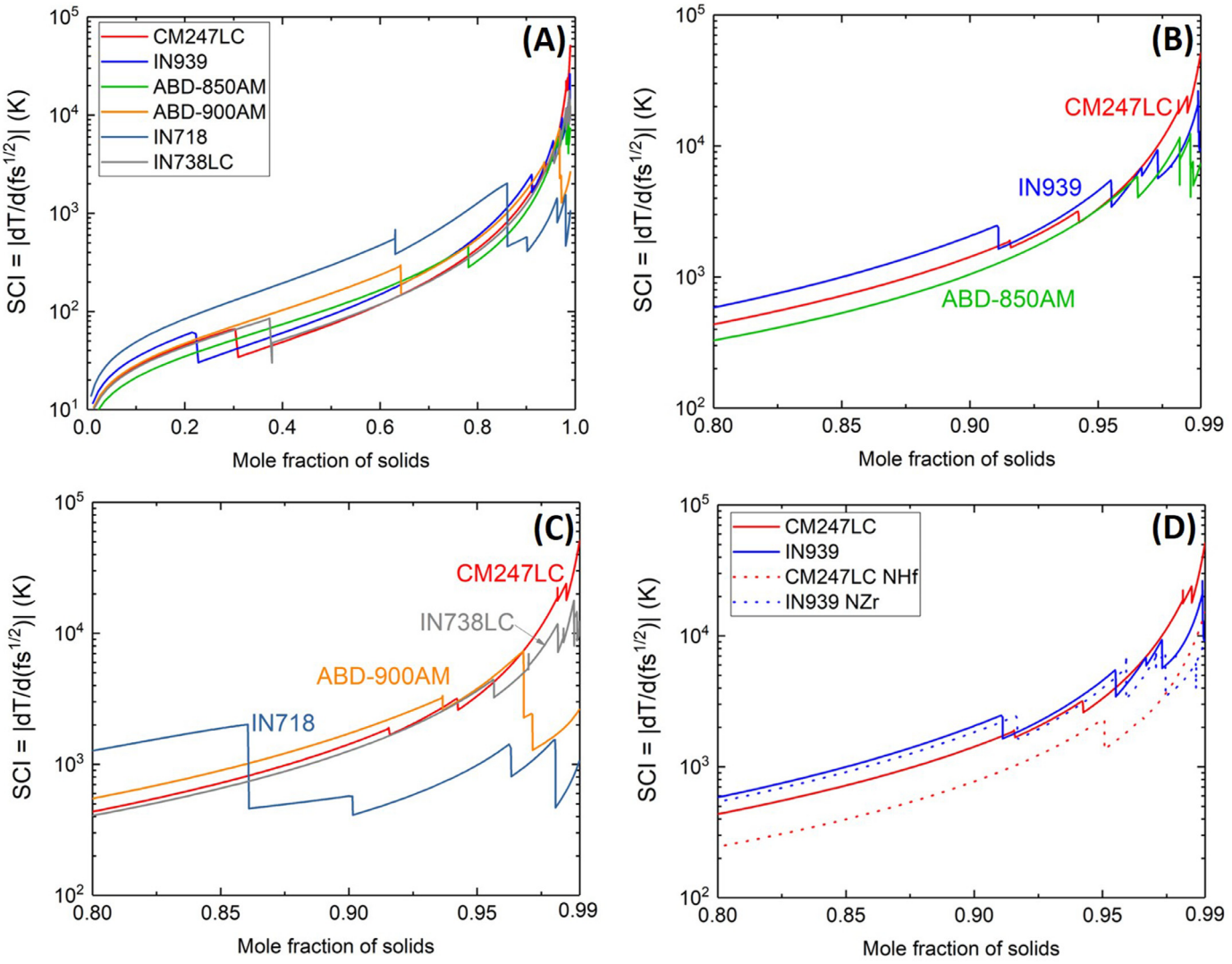

Fig. 11. Solidification cracking index (SCI) of various alloys based upon solidification curves calculated using Thermo-Calc with TTNi8 database. (a) SCI value over the full range of solid fraction, (b, c & d) SCI value of the last stage solidification in the range of 0.8–0.99 of CM247LC, IN939, ABD-850AM, ABD-900AM, IN718, IN738LC, CM247LC Hf free and IN939 Zr free.

Table 6
Solidification cracking index (SCI) values for various alloys calculated based upon prediction made using Scheil solidification curves by Thermo-Calc with TTNi8 database. Freezing ranges obtained from both Scheil and equilibrium solidification are also presented. The specific composition used in the calculations are provide in supplementary data (phase selection 1).

	SCI (K)			Freezing range (K)	
	f_s = 0.8-0.9	f_s = 0.9-0.99	f_s = 0.8-0.99	Scheil	Equilibrium
ABD-850AM	647	5545	4799	266	91
CM247LC	875	15980	14109	392	87
IN939	1247	7170	5922	343	182
IN718	1459	921	1261	264	174
IN738LC	787	6681	5711	286	99
ABD-900AM	1076	3577	2885	268	101
CM247LC Hf free	479	5036	4295	184	76
IN939 Zr free	1123	4352	3568	282	150

strict liquid flow down liquid channels to feed shrinkage. Also, no effect of microstructure is considered: a combination of low texture strength and small grain size of ABD-850AM might facilitate more efficient liquid filling and stress alleviation from rapid solidification [58,59]. Such possible effects need more research to explore and can lead to development of improved cracking indices for the ABD approach.

5.2. High temperature ductility on solid-state cracking

A solid-state mechanism is also shown to be responsible for some of the cracking observed in CM247LC and IN939. This effect is exacerbated by γ' precipitation which compromises local ductility. Although the instantaneous cooling rate for SLM is extremely high – estimated at 10^{6-7} K/s [60,61] – the repeated thermal cy-

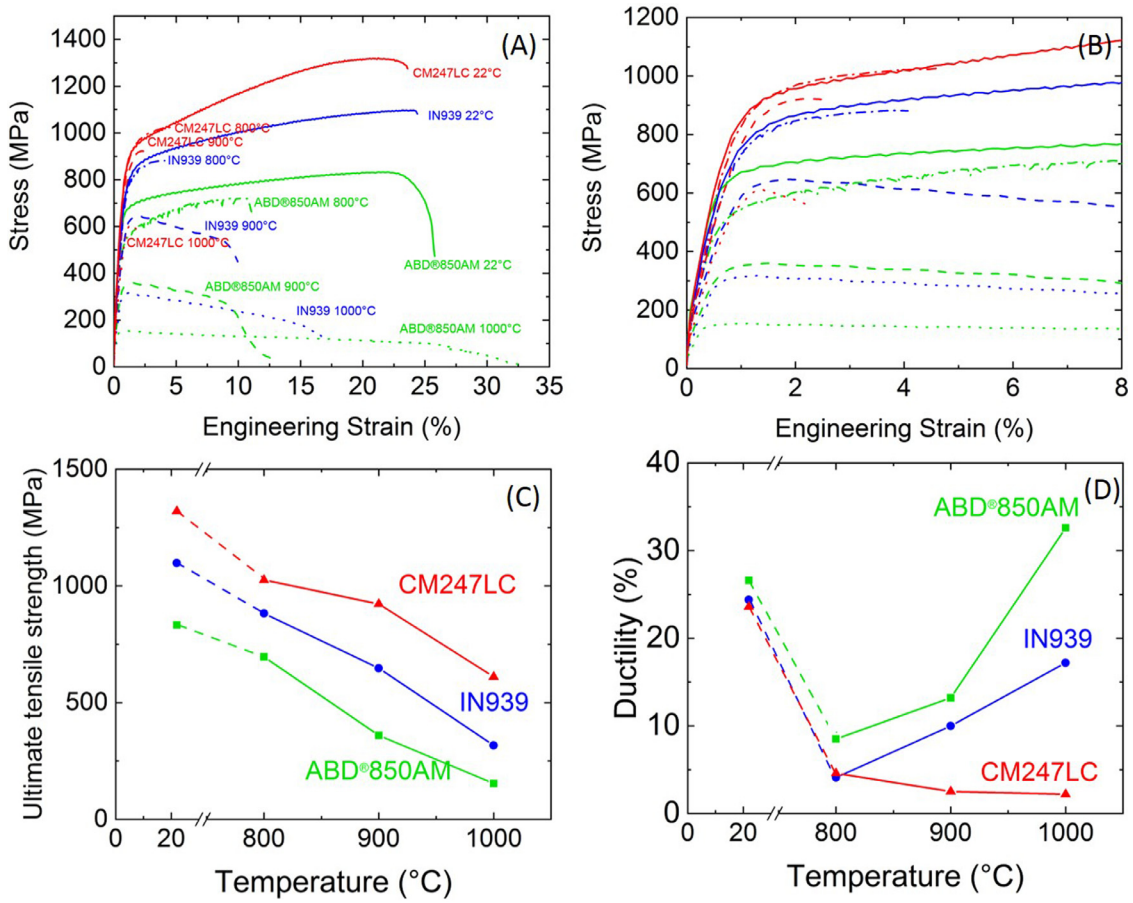

Fig. 12. Results of ETMT tensile tests at room temperature and between 800–1000 °C in as-fabricated state. (a) Engineering stress-strain curves for all tests at a strain rate of $10^{-2}s^{-1}$, (b) a magnified view of curves (0–8 % strain), (c-d) illustrate the ultimate tensile strength and ductility values for the three alloys. Note, anomalous yield behaviour is observed for ABD-850AM at 800 °C where fracture occurred outside the gauge section, hence the ductility measurement was an underestimation.

cles as the laser beam traverses (commonly known as the intrinsic heat treatment effect) can play a significant role in tailoring properties [62]. The formation of γ' precipitates in the as-fabricated microstructure needs to be limited, as the temperature window that promotes it can be reached multiple times through the AM build. In general, less laser overlap during building can reduce the thermal loading, hence lower the propensity to strain ageing [63]. The SAC index presents an estimate of this cracking tendency by summing all γ' approximately averaged by their atomic fraction. Although an empirical metric, it demonstrates a strong positive correlation with the chemical driving force for γ' precipitation as predicted by Thermo-Calc, see the Appendix.

Another critical factor is the ductility dip phenomenon. A trade-off of strength and ductility also occurs in the relevant temperature regime of 800–1000 °C. High performance alloys such as Udimet 720Li and RR1000 possess a ductility minimum of around 3 % or less [64]. Hence further evaluation of tensile response of the alloys used in the present study have been conducted in the susceptible temperature regime. To ensure the testing is as representative as possible to the AM process, the heating and deformation time were kept to a minimum ($<$ 30 seconds), so little effect on the microstructure will arise due to *in-situ* heating. The tensile results – including stress-strain curves, UTS and ductility plots – are shown in Fig. 12(a–d). All alloys displayed a decreasing UTS with increasing temperature; the room temperature strength level exhibits the same trend as observed with hardness measurements in Fig. 10. The results confirm that over the temperature range tested, a minimum in ductility is indeed present at ~ 800 °C for IN939 and ABD-850AM, whereas the ductility of CM247LC decreased monotonically with temperature, presumably due to its very high γ' solvus (~ 1250 °C).

In conclusion, the ABD-850AM alloy consistently shows the lowest γ' precipitation propensity of the alloys tested, and also possesses the highest value of elongation at the ductility minimum. Moreover, the weak texture strength and smaller grain size – which are dictated by the intrinsic thermophyisical parameters of the composition [60] – might also assist in homogeneous stress distribution [10] and alleviate the cracking susceptibility. Consequently these factors rationalise ABD-850AM's greater resistance to solid-state cracking during additive manufacturing.

5.3. Potency of liquation sources: γ/γ' eutectic and MC carbides

Liquation cracking relies upon two critical factors: formation of a localised liquid film and the presence of tensile stress. Therefore, it is frequently seen in the heat-affected zone (HAZ) during welding – local phases being melting by reheating from previous layers acting together with a shrinkage strain.

DSC data can provide a good indication of the susceptibility to liquation susceptibility since the solidus transition during heating is measured. For example, neither CM247LC nor IN939 exhibit a sharp onset of melting, during heating. This type of behaviour seen in the DSC reflects significant nanosegregation within cells (submicron scale) in the latter stages of freezing, as confirmed by spec-

troscopy experiments [12,14]. Locations such as cellular/dendritic boundaries thus have lower melting points compared to the bulk due to MC-type carbide/nitride [45], Laves phase [65] and γ/γ' eutectic [66], which are liquation sources. Moreover, intense thermal stresses that build up from the SLM process [17,27] can provide mechanical driving force to open up cracks. In contrast, ABD-850AM exhibits a sharp melting onset at 1330 °C. This indicates that the solidified cells/dendrites have a relatively uniform composition even in the last-to-solidify region and so significant melting begins at a well-defined temperature. It agrees with the microscopy analysis that neither carbide or γ/γ' eutectic were observed, meaning a low capacity to form liquid films during reheating. Therefore, the unique microstructure of the ABD-850AM alloy reflects a significantly reduced nanosegregation and phase formation that prevents liquation cracks.

From the analysis above, it is not difficult to understand why CM247LC suffers from liquation, whereas ABD-850AM does not. But the same argument cannot fully interpret the case of IN939 – for which we found no definitive evidence of liquation cracks. In fact, CM247LC shows a distinctive feature of γ/γ' eutectic in the inter-dendritic/cellular regions and its volume fraction appears to be much larger than carbide phases. It is therefore considered that γ/γ' eutectic is a more potent liquid former in this case – despite carbide in IN939 predicted with higher volume fraction and a rather broadened liquidus point being captured by DSC. The reason why the effect of carbide may not seem as potent might due to its small size. As Dye et al. have reported, the liquation propensity is a strong function of carbide size: larger carbides promote more pronounced liquation [45]. The size of carbides based on their microscopy analysis in conventional manufacture is usually ~ 2 μm, whereas in the current study, the carbide sizes are suppressed by SLM to about ~ 100 nm. Although we cannot rule out the possibility of liquation cracks in IN939 (promoted by carbide), it is believed that γ/γ' eutectic can be more detrimental in the context of SLM.

On the other hand, the eutectic pools in CM247LC were revealed both in grain boundaries and cell boundaries in the as-fabricated microstructure, yet no cracking were observed in the latter. This is due to the high coherency of cells within a grain, which they can thermally expand or contract in a similar direction, whereas the grain boundaries are not coherency. The contraction between adjacent grains can provide driving force and makes it vulnerable to liquation cracks. Moreover, the mis-orientations among the grains promotes easier solute enrichment which forms a more potent eutectic pool. The tendency of forming liquid from remelting is higher than from cell boundaries.

6. Implications to alloy design efforts and one further design iteration

The promising results reported thus far have allowed another alloy design iteration to be carried out termed ABD-900AM. The alloy is designed by further reducing the SCI value to resist solidification cracking while increasing the γ' fraction by 10 %. Its location in the design space is shown in Fig. 1. Although the magnitude of freezing range is comparable to ABD-850AM, its SCI value has been reduced, see Table 6. To validate the processibility, the alloy was fabricated using the same conditions described in Section 3.2 and the microstructure developed is illustrated in Fig. 13(a–c). There are only a few short cracks observed in the corners (border), where the macroscopic tensile stress is the highest, but no cracks are observed in the bulk. With further optimisation in laser parameters, such as scanning speed and hatch distance, it was possible to produce cracking free microstructure [37]. EBSD measurements have determined the grain size to be 32 μm with the {1 0 0} texture strength of 4.1. Fig. 13 illustrates that a bimodal distribution of γ' can be generated via heat treatment, see Table 2.

The mechanical properties of the new ABD-850AM and ABD-900AM superalloys in the fully heat treated conditions have been assessed at various temperatures, and plotted together with heritage alloys CM247LC and IN939 in Fig. 13 (d & e). ABD-900AM demonstrates higher yield strength over ABD-850AM and IN939 right up until close to the γ' solvus temperature. IN939 possesses high strength just below γ' solvus which is believed to be due to its very high carbon content (0.16 wt. %), which is crucial for grain boundary cohesion and creep performance [67]. Furthermore, ABD-900AM shows superior yielding behaviour to CM247LC up to 700 °C, at which point the trend is then reversed at higher temperatures due to their large differences in γ' fraction (~ 30%). Obviously, due to large degree of cracking, CM247LC may not be suitable for critical components despite good strength. It is worth noting that ABD-850AM has lost ductility significantly after heat treatment. This is due to its rather low C & B content that weakens grain boundaries, an effect which becomes more pronounced when the grain interior is significantly strengthened during intergranular dominated deformation. Therefore, to recover the high temperature ductility, a modified version of ABD-850AM with intentional addition of carbon (0.045 wt%) and boron (0.005 wt%) has been produced, whilst keeping other elements unchanged. No compromised printability was found from the processing trials [37], yet the hot ductility was markedly improved to over 25% after heat treatment. ABD-900AM was designed with the same philosophy with intentional carbon addition, whilst its high temperature elongation was also maintained (over 15%).

Finally, one should note that nickel-superalloys are high temperature materials and therefore one should consider their creep performance. Thus we have conducted preliminary ASTM creep tests at various conditions with the ABD-900AM alloy. The same measurements were made with two other popular heritage alloys by additive manufacturing, i.e. IN718 and CM247LC. The former can be readily printed without cracks [33,34] whilst exhibiting reasonable strength. The latter is the-state-of-art alloy containing ~ 65% γ' fraction, but generally not printable, as demonstrated in this paper and by other researchers [11,12]. All materials are fully heat treated see Table 2. The creep tests were carried out by Element Materials Technology Ltd. with testing performed consistent with ASTM standards. The testing temperatures were selected between 700–980 °C and applied stress range from 200–600 MPa. A Larson-Miller Parameter (LMP) plot was generated to rationalise the overall creep resistance of the alloys across different conditions, defined as

$$\mathrm{LMP} = \mathrm{T} \times (20 + \log_{10}(\mathrm{t_r})/1000) \quad (2)$$

where T is absolute temperature in Kelvin and $\mathrm{t_r}$ is time to rupture in hours.

Fig. 14 illustrates the LMP data generated in this way. It is clear that IN718 has the lowest resistance to creep among the three alloys tested. However, one should note that its high iron content makes it susceptible to oxidation during longer exposures at higher temperatures, also the instability of γ'' intermetallic at intermediate-high temperature regime severely weakens the microstructure [68]. ABD-900AM demonstrates a marked improvement over IN718, particularly at the high temperature, low stress regime (900 °C/200 MPa). This is due to the improved oxidation resistance and stability of γ' strengthening phase, but also its great printability to prevent crack assisted damage. However, CM247LC performed the best among the three, although the microstructure is largely impaired due to cracking. The very high γ' content pro-

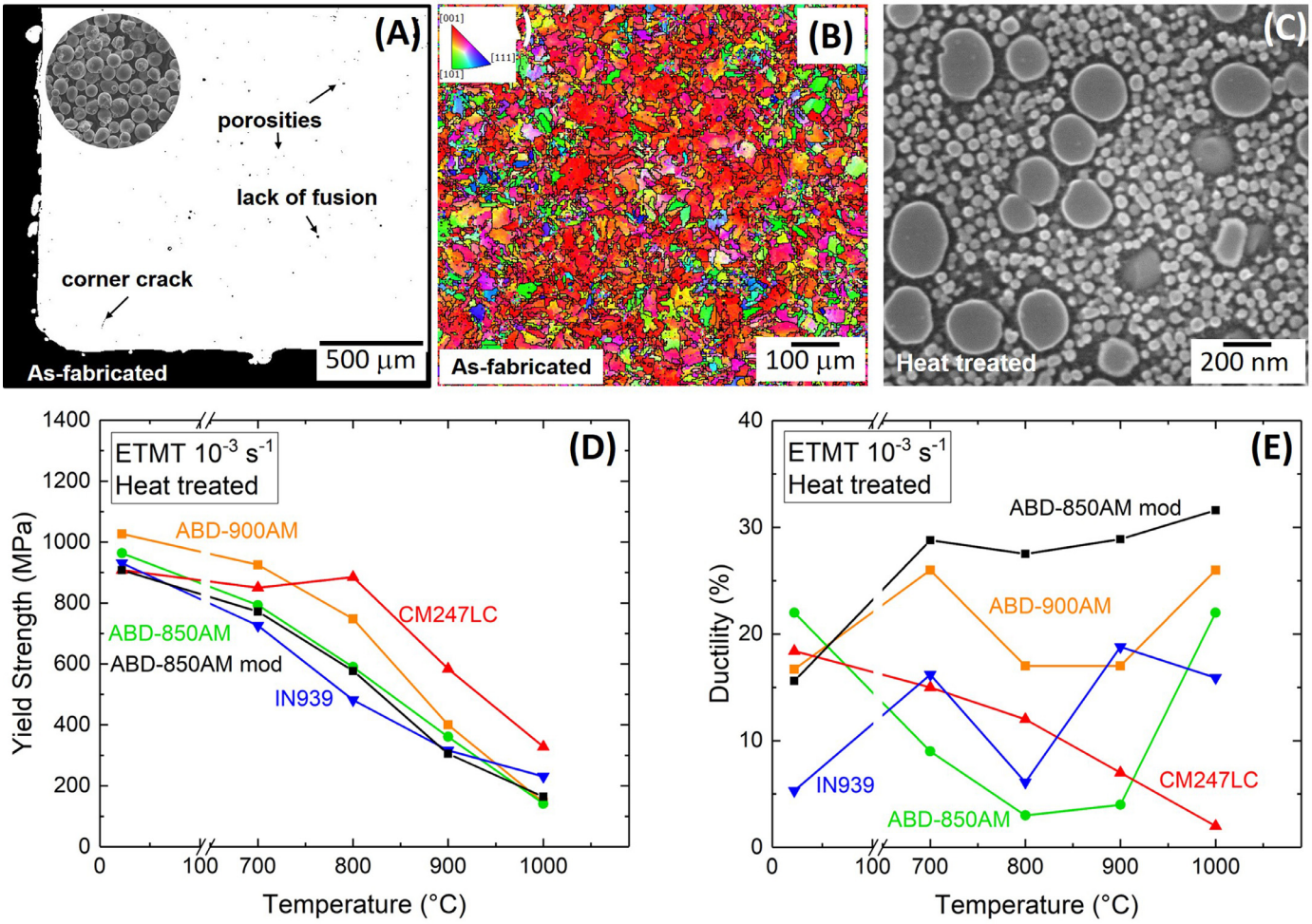

Fig. 13. As-fabricated microstructure and mechanical properties determined from ETMT tensile tests of ABD-900AM. (a) the powder characterisation and digitised SEM image, (b) IPF-Z map along building direction, (c) bimodal distribution of γ' in full heat treatment condition. (d & e) shows yield strength and ductility of CM247LC, IN939, ABD-850AM, ABD-850AM mod and ABD-900AM obtained from ETMT tensile tests at a strain rate of $10^{-3}s^{-1}$ at various temperatures in the heat-treated state. The heat treatment conditions is given in Table 2.

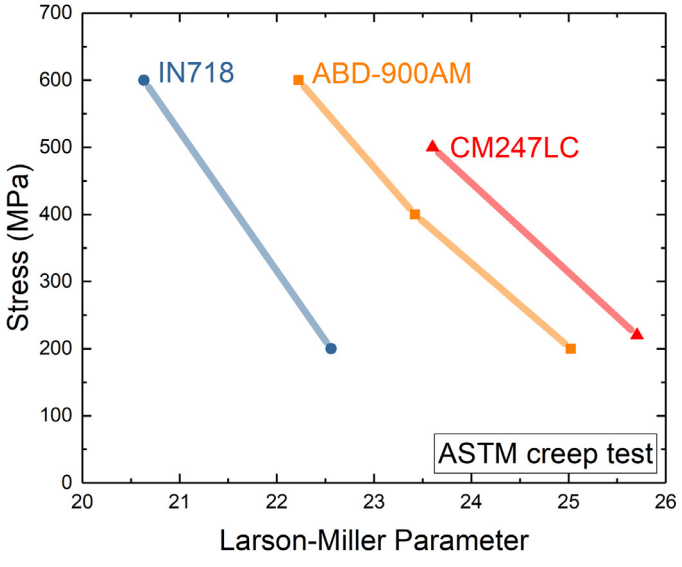

Fig. 14. Larson-Miller parameter plot of heat treated IN718, ABD-900AM and CM247LC tested according to ASTM standards.

motes its creep life, yet it is markedly lower than when produced by the investment casting route [11].

To conclude, the alloy design approach presented here has opened an avenue for designing new grades of superalloys that are suitable for additive manufacturing. It does not seem likely that existing heritage alloys – which were designed for conventional processes such as investment casting – are well matched to the new AM process. After all, new processing techniques usually usher in further alloy design efforts, such that the composition/processing/property relationship is optimised.

7. Summary and conclusions

The following specific conclusions can be drawn from this work:

1. The inter-relationship between alloy composition, processability and mechanical behaviour in additively manufactured nickel-based superalloys has been studied, with emphasis on the heritage alloys IN939 and CM247LC but also two newly-designed superalloys designated ABD-850AM and ABD-900AM. The new alloys have been isolated using a design-based modelling approach, taking into account the requirement for adequate processability but also the property levels needed.

2. In our experimentation on a broad range of alloy compositions, various forms of manufacturing-related defect have been observed: solidification cracking, liquation cracking and solid-state (sometimes referred to as strain-age coupled ductility dip) cracking; however the susceptibility to each varies from alloy to alloy. Solidification and solid-state cracking occur in both heritage alloys, but liquation cracking is observed only in CM247LC. The newly-designed alloys are largely defect-free in the geometries printed, for the processing conditions employed here.
3. In reaching the above conclusion, it has been necessary to be clear on defect formation characteristics. Solidification cracking, when it is found, is typified by exposed cells/dendrites. Sites of liquation cracks are associated with low melting point γ/γ' eutectic pools which have at some point been in contact with liquid films. By way of contrast, solid-state cracks can be sharply kinked and long that extend over depths of many meltpools.
4. When an alloy is prone to defect formation, its occurrence is location-dependent. The surfaces of the 3D geometries printed are associated with the highest crack density, the most pronounced texture and the greatest grain size. Their magnitudes decrease as one moves into the centre, towards the bulk, and away from the borders. This finding confirms a strong dependency upon the local stress state developed.
5. It is likely that there are various contributory factors to the improved processing displayed by the new alloys. First, a freezing range which is narrower with limited intergranular particle precipitation can decrease the susceptibility to solidification cracking. Second, the absence of low melting point eutectic pools – which are otherwise observed in the likes of CM247LC – prevents liquation in the heat-affected regions. Finally, the engineering of sufficient high temperature ductility for resisting solid-state cracking; this has been achieved by lowering the temperature for – and extent of – γ' precipitation.
6. Via the alloy design process, it has proven possible to approach the low-temperature strength of CM247LC, whilst improving markedly the processability. However, the need to restrict the solidification range – by limiting the elements which promote precipitation of the γ' phase, but also concentrations of the grain boundary strengthening metalloids C and B coupled with the small grain size developed – means that the creep performance at the highest temperatures is somewhat compromised.
7. The findings confirm that existing heritage alloys – which were not designed with additive manufacturing in mind – have compositions which are not the most suitable for this new process, and that new alloy compositions can be designed which are demonstrably superior to them, whilst demonstrating sound mechanical properties. Nevertheless, further experimentation is needed to confirm unambiguously the relative potencies of the factors which confer the improved processing.

Declaration of competing interest

The authors declare that they have no known competing financial interests or personal relationships that could have appeared to influence the work reported in this paper.

Acknowledgements

The authors acknowledge funding from Innovate UK, formerly the Technology Strategy Board (TSB), under project number 104047, and specifically the Materials and Manufacturing Division. They appreciate inspiring discussions with Dr. Ravi Aswathanarayanaswamy of Renishaw plc. Helpful comments from Dr. Jitendra Patel and Dr. Robin Wilson of Innovate UK are acknowledged. C.P. would like to acknowledge the funding from Innovation Fellowship funded by Engineering and Physical Science Research Council (EPSRC), UK Research and Innovation, under the grant number: EP/S000828/1.

Appendix

The alloy design approach used has most strongly emphasised estimates of (i) the freezing range and (ii) the strain-age cracking index. In what follows, we provide further detail to our calculations, emphasising particularly the source of systematic error which we believe to be present. To facilitate transparency, a Data-In-Brief (supplementary data) is provided which gives details of the computations which can be then repeated by others.

The solidification path was calculated using the Thermo-Calc software using the Scheil module and TTNi8 database, at a temperature step size of 0.5 K. The phases selected for inclusion in the calculations were guided by literature observations for phases known to play a role in AM-produced microstructures: γ' [14], η [71], δ [72], Laves [73], borides [19], carbides [14] and Ni_5M intermetallic in addition to liquid and γ matrix. The phase descriptors enabled in the calculations are: 'LIQUID', 'FCC_A1', 'GAMMA_PRIME', 'LAVES', 'ETA', 'DELTA', 'M3B2_TETR', 'NI5M', 'M23C6' and 'HCP_A3'. To clarify, 'FCC_A1' includes both γ matrix and MC carbide. The readers are refereed to the supplementary data for composition input and results.

The freezing range (ΔT) has been defined as the temperature difference between the γ phase formation temperature (with supersaturated carbon as solid solution) and a fraction of solid corresponding to $f_s = 0.99$. For the majority of the cases, the γ phase formation temperature corresponds to $f_s = 0$, but for a few exceptions – for example IN100 – the carbide formation temperature is predicted to be higher than the liquidus temperature thus causing a sharp discontinuity at $f_s = 0$; here the γ phase formation temperature is used instead of $f_s = 0$. Hence the equation can be written as

$$\Delta T = T_{f_\gamma} - T_{f_s=0.99} \tag{A1}$$

The Scheil solidification analysis gives different results dependent upon the assumptions made in the thermodynamic database. We believe that three systematic uncertainties are introduced by virtue of (1) the selection of phases included for calculations, (2) the choice of thermodynamic database and (3) the variation in the allowable composition ranges inherited from the different materials suppliers and patents.

Fig. A.1 shows the predicted freezing ranges of a set of alloys calculated by enabling (i) the 10 selected phases described above, and alternatively (ii) all default phases. A general trend is found: the magnitude of the freezing ranges being narrowed by the formation of more phases. This is because during the solidification process, in particular where f_s is greater than 0.9, phase formation helps to consume the excessive rejected solute in the interdendritic liquid. For the alloys plotted, an average difference of 33 K is induced by the choice of phases. Phase formation appears as a discontinuity in the phase fraction/temperature curves. However – and importantly for our alloy design effort – broadly speaking, the rank order of the alloys when judged on this basis is largely unaffected by the list of phases included.

Next, Fig. A.1(b & c) illustrate the influence of database choice: results from TTNi8 (b) are compared to those from TCNI8 (c) whilst enabling all phases by default. This time, no general trend of narrowing or broadening the freezing range is found, yet the magnitude of freezing range change is found to be larger with an average difference of 39 K. Nevertheless, the hard-to-print alloys – for example CM247LC or IN792 – always possess relatively large predicted freezing ranges, and easy-to-print alloys – for example IN625 and IN718 – illustrate reasonably low freezing ranges. For avoidance of doubt, though IN738LC obtains marginally lower

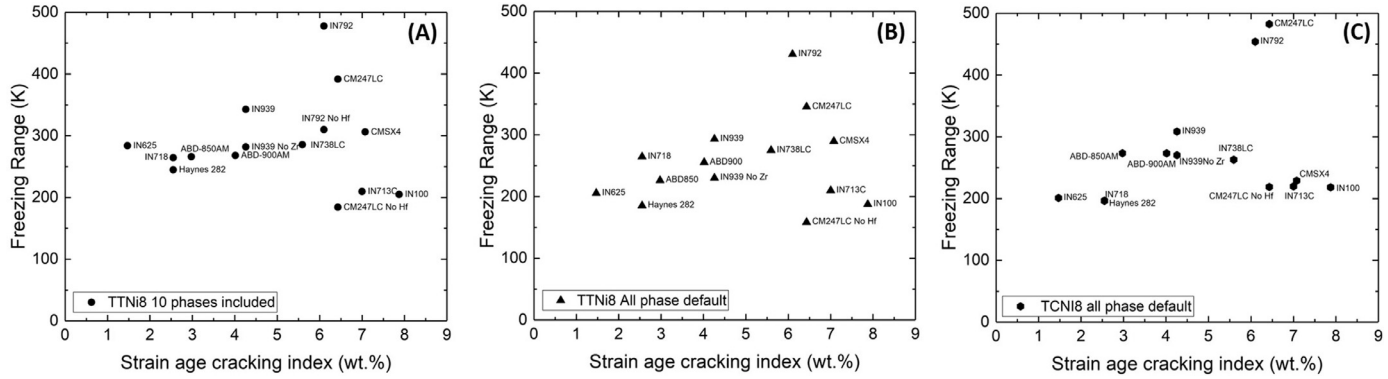

Fig. A.1. Freezing range as a function of strain age cracking index for some heritage alloys using different databases and choice of phases. (a) TTNi8 database with phase selection consistent with the manuscript, (b) TTNi8 database with all default phases, (c) TCNI8 database with all default phases.

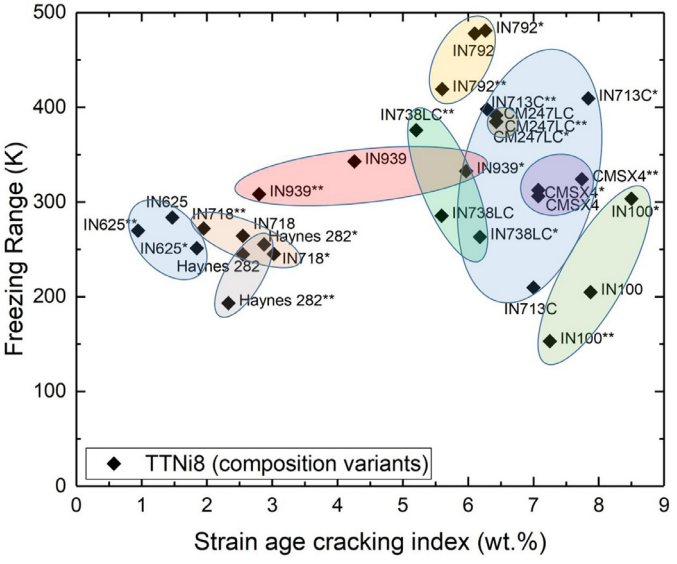

Fig. A.2. Variation of freezing range and SAC index as a function of composition variants in the specification ranges. Single and double asterisks refer to two possible compositions detailed in supplementary data.

freezing range than ABD alloys only in the TCNI8 database, the SCI analysis for the last stages of solidification (with TCNI8 database) still shows both ABD alloys obtaining much lower indices (3089 & 2781 K) vs IN738LC (4651 K). Consequently, ABD-850AM and ABD-900AM can be unfailingly distinguished from the very large compositional bank regardless of the selection of phases and/or database.

In addition, the effect on the freezing range of the allowable compositional range is also considered. This is very relevant to the practitioners in the field because the commercial alloys are usually specified within a range of compositions as well as some tolerance of impurities.Unsurprisingly, the level of minor element tolerance for some alloys can impose a dramatic change in additive manufacturability [74]. The range of compositions used for calculations are taken from technical data sheets where available (see supplementary data-in-brief). To avoid confusion, the calculations were completed based upon solely on the possible compositional ranges, hence may not necessarily capture the largest difference in the freezing range. Fig. A.2 demonstrate the possible locations of each alloy in the design space using the TTNi8 database with phase selections consistent with the manuscript, based upon maximum, minimum and recommended compositions. It is clear that some alloys are very sensitive to compositional variation, including IN738LC, for which the freezing range has changed by over 100 K and SAC by ~ 1. However, for others alloys the freezing range can be generally insensitive such as IN718, by less than 30 K. The key point here is that the estimate of the freezing range possesses an uncertainty related as much to the specification of alloy composition as to the method of calculation and errors in the underlying data.

The second parameter which has been used widely in this work is the strain age cracking (SAC) index which describes the propensity of forming γ' precipitates during the so-called "intrinsic heat treatment" – which is repeated reheating and cooling arising from the AM fabrication. The formation of γ' compromises local ductility via effective total fraction of γ' forming elements: Al, Ti, Nb and Ta (wt.%) as acknowledged by Thompson et al. [75], Henderson et al. [76]. The index is hence expressed in this work as

$$M_{SAC} = [Al] + 0.5[Ti] + 0.3[Nb] + 0.15[Ta] \quad (3)$$

The empirical strain age cracking index provides only a first approximation to a very difficult problem. However, to validate its use – and in the absence of any accurate composition-dependence model for overall transformation kinetics in the nickel-based superalloys – the chemical driving force for γ' precipitation in some heritage alloys has been calculated using Thermo-Calc with TTNi8 database. Fig. A.3 shows the γ' precipitation driving force as a function of SAC index in the temperature range of 800–1000 °C. It is clear that all alloys possess very high chemical driving force to form precipitates if the undercooling is large, as expected, for example at 800 °C, but then no correlation with SAC is found. However, at high temperatures for example 1000 °C, a strong positive correlation between SAC index and precipitation driving force is found; the correlation coefficient is R = 0.91 and the interpolation of the linear fitting is through the origin. The result implies a thermodynamics basis of the SAC index. In principle, the adoption of a new index using chemical driving force would be a step forward further than the SAC index, however to be clear, the contribution of interfacial energy that facilitates precipitation is not considered. This may be a reasonable approximation, because the interfacial energy for nickel-based superalloys is exceptionally low – typically on the order of 0.01 Jm^{-2} [77,78], which is about one-two orders of magnitude less than other f.c.c. alloy systems, for example the Co-Cu and Al-Cu system [77,79]. Further work is needed to explore these ideas.

Additional sub models used for example estimating strength, creep and microstructural stabilities were taken from the literatures [23–25] with no further improvisation. Hence not detailed in the appendix.

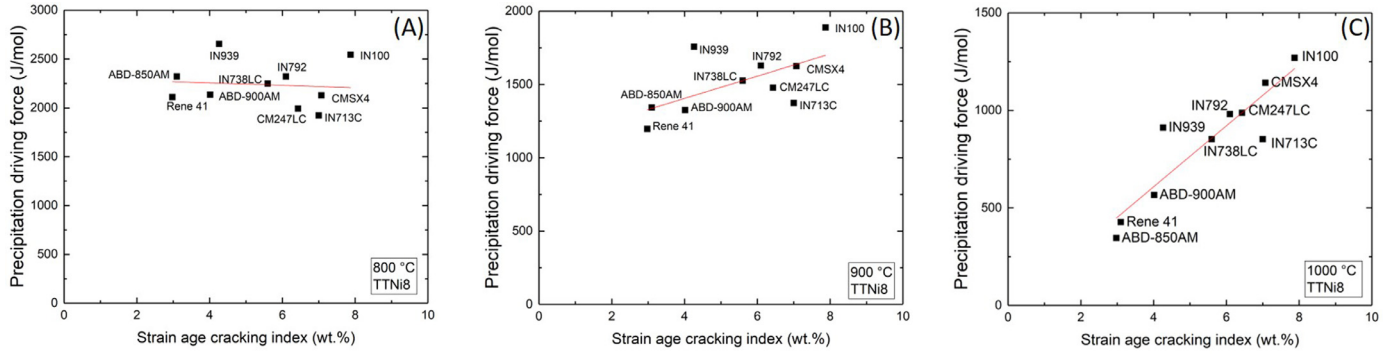

Fig. A.3. Illustration of the correlation of precipitation driving force at 800–1000 °C with strain age cracking index.

Supplementary material

Supplementary material associated with this article can be found, in the online version, at doi:10.1016/j.actamat.2020.09.023.

References

[1] R.C. Reed, C.M.F. Rae, 22 - Physical metallurgy of the nickel-based superalloys, in: D.E. Laughlin, K. Hono (Eds.), Physical Metallurgy, 5th ed., Elsevier, Oxford, 2014, pp. 2215–2290.

[2] D.D. Gu, W. Meiners, K. Wissenbach, R. Poprawe, Laser additive manufacturing of metallic components: materials, processes and mechanisms, Int. Mater. Rev. 57 (3) (2012) 133–164.

[3] R.R. Dehoff, M.M. Kirka, W.J. Sames, H. Bilheux, A.S. Tremsin, L.E. Lowe, S.S. Babu, Site specific control of crystallographic grain orientation through electron beam additive manufacturing, Mater. Sci. Technol. 31 (8) (2015) 931–938.

[4] C. Körner, Additive manufacturing of metallic components by selective electron beam melting–a review, Int. Mater. Rev. 61 (5) (2016) 361–377.

[5] D. Herzog, V. Seyda, E. Wycisk, C. Emmelmann, Additive manufacturing of metals, Acta Mater. 117 (2016) 371–392.

[6] Y.M. Wang, T. Voisin, J.T. McKeown, J. Ye, N.P. Calta, Z. Li, Z. Zeng, Y. Zhang, W. Chen, T.T. Roehling, R.T. Ott, M.K. Santala, P.J. Depond, M.J. Matthews, A.V. Hamza, T. Zhu, Additively manufactured hierarchical stainless steels with high strength and ductility, Nat. Mater. 17 (2017) 63–70.

[7] I. Todd, Metallurgy: printing steels, Nat. Mater. 17 (2018) 13–14.

[8] C. Qiu, M. Attallah, X. Wu, P. Andrews, Influence of hot isostatic pressing temperature on microstructure and tensile properties of a nickel-based superalloy powder, Mater. Sci. Eng. A 564 (2013) 176–185.

[9] R. Cunningham, C. Zhao, N. Parab, C. Kantzos, J. Pauza, K. Fezzaa, T. Sun, A.D. Rollett, Keyhole threshold and morphology in laser melting revealed by ultrahigh-speed x-ray imaging, Science 363 (6429) (2019) 849–852.

[10] J.H. Martin, B.D. Yahata, J.M. Hundley, J.A. Mayer, T.A. Schaedler, T.M. Pollock, 3D Printing of high strength aluminium alloys, Nature 549 (21) (2017) 365–369.

[11] L.N. Carter, Selective Laser Melting of Nickel Superalloys for High Temperature Applications, University of Birmingham, 2013 Ph.D. thesis.

[12] V. Divya, R. Muñoz-Moreno, O. Messé, J. Barnard, S. Baker, T. Illston, H. Stone, Microstructure of selective laser melted CM247LC nickel-based superalloy and its evolution through heat treatment, Mater. Charact. 114 (2016) 62–74.

[13] N.J. Harrison, I. Todd, K. Mumtaz, Reduction of micro-cracking in nickel superalloys processed by selective laser melting: a fundamental alloy design approach, Acta Mater. 94 (2015) 59–68.

[14] X. Wang, L.N. Carter, B. Pang, M.M. Attallah, M.H. Loretto, Microstructure and yield strength of SLM-fabricated CM247LC Ni-superalloy, Acta Mater. 128 (2017) 87–95.

[15] J. Xu, H. Gruber, D. Deng, R.L. Peng, J.J. Moverare, Short-term creep behavior of an additive manufactured non-weldable nickel-base superalloy evaluated by slow strain rate testing, Acta Mater. 179 (2019) 142–157.

[16] N.J. Harrison, Selective Laser Melting of Nickel Superalloys: Solidification, Microstructure and Material Response, The University of Sheffield, 2016 Ph.D. thesis.

[17] E. Chauvet, P. Kontis, E.A. Jägle, B. Gault, D. Raabe, C. Tassin, J.-J. Blandin, R. Dendievel, B. Vayre, S. Abed, G. Martin, Hot cracking mechanism affecting a non-weldable Ni-based superalloy produced by selective electron beam melting, Acta Mater. 142 (2018) 82–94.

[18] J.H. Boswell, D. Clark, W. Li, M.M. Attallah, Cracking during thermal post-processing of laser powder bed fabricated CM247LC Ni-superalloy, Mater. Des. 174 (2019) 107793.

[19] P. Kontis, E. Chauvet, Z. Peng, J. He, A.K.d. Silva, D. Raabe, C. Tassin, J.J. Blandin, S. Abed, R. Dendievel, B. Gault, G. Martin, Atomic-scale grain boundary engineering to overcome hot-cracking in additively-manufactured superalloys, Acta Mater. 177 (2019) 209–221.

[20] B. Attard, S. Cruchley, C. Beetz, M. Megahed, Y. Chiu, M. Attallah, Microstructural control during laser powder fusion to create graded microstructure Ni–superalloy components, Addit. Manuf. 36 (2020) 101432.

[21] W. Zhou, G. Zhu, R. Wang, C. Yang, Y. Tian, L. Zhang, A. Dong, D. Wang, D. Shu, B. Sun, Inhibition of cracking by grain boundary modification in a non-weldable nickel-based superalloy processed by laser powder bed fusion, Mater. Sci. Eng. A 791 (2020) 139745.

[22] C. Panwisawas, Y.T. Tang, R.C. Reed, Metal 3D printing as a disruptive technology for superalloys, Nat. Commun. 11 (2327) (2020).

[23] R.C. Reed, T. Tao, N. Warnken, Alloys-by-design: application to nickel-based single crystal superalloys, Acta Mater. 57 (19) (2009) 5898–5913.

[24] R. Reed, Z. Zhu, A. Sato, D. Crudden, Isolation and testing of new single crystal superalloys using alloys-by-design method, Mater. Sci. Eng. A 667 (2016) 261–278.

[25] D. Crudden, A. Mottura, N. Warnken, B. Raeisinia, R. Reed, Modelling of the influence of alloy composition on flow stress in high-strength nickel-based superalloys, Acta Mater. 75 (2014) 356–370.

[26] A.A.N. Németh, D.J. Crudden, D.M. Collins, V. Kuksenko, C.H. Liebscher, D.E.J. Armstrong, A.J. Wilkinson, R.C. Reed, On the influence of Nb/Ti ratio on environmentally-assisted crack growth in high-strength nickel-based superalloys, Metall. Mater. Trans. A 49 (9) (2018) 3923–3937.

[27] T. DebRoy, H. Wei, J. Zuback, T. Mukherjee, J. Elmer, J. Milewski, A. Beese, A. Wilson-Heid, A. De, W. Zhang, Additive manufacturing of metallic components – process, structure and properties, Prog. Mater. Sci 92 (2018) 112–224.

[28] W.E. Frazier, Metal additive manufacturing: a review, J. Mater. Eng. 23 (6) (2014) 1917–1928.

[29] M. Cloots, P.J. Uggowitzer, K. Wegener, Investigations on the microstructure and crack formation of IN738LC samples processed by selective laser melting using Gaussian and doughnut profiles, Mater. Des. 89 (2016) 770–784.

[30] X. Zhang, H. Chen, L. Xu, J. Xu, X. Ren, X. Chen, Cracking mechanism and susceptibility of laser melting deposited Inconel 738 superalloy, Mater. Des. 183 (2019) 108105.

[31] A. Hariharan, L. Lu, J. Risse, A. Kostka, B. Gault, E.A. Jägle, D. Raabe, Misorientation-dependent solute enrichment at interfaces and its contribution to defect formation mechanisms during laser additive manufacturing of superalloys, Phys. Rev. Mater. 3 (2019) 123602.

[32] H. Qi, M. Azer, A. Ritter, Studies of standard heat treatment effects on microstructure and mechanical properties of laser net shape manufactured INCONEL 718, Metall. Mater. Trans. A 40 (2009) 2410–2422.

[33] Y. Chen, K. Zhang, J. Huang, S.R.E. Hosseini, Z. Li, Characterization of heat affected zone liquation cracking in laser additive manufacturing of Inconel 718, Mater. Des. 90 (2016) 586–594.

[34] L. Johnson, M. Mahmoudi, B. Zhang, R. Seede, X. Huang, J.T. Maier, H.J. Maier, I. Karaman, A. Elwany, R. Arróyave, Assessing printability maps in additive manufacturing of metal alloys, Acta Mater. 176 (2019) 199–210.

[35] A.S. Shaikh, Development of a γ' Precipitation Hardening Nickel-Base Superalloy for Additive Manufacturing, Chalmers University of Technology, 2018 Master's thesis.

[36] R. Aswathanarayanaswamy, Private communication on optimal processing conditions of CM247LC, Renishaw Plc, 2018.

[37] J.N. Ghoussoub, Y.T. Tang, C. Panwisawas, A.A. Németh, R.C. Reed, On the influence of alloy chemistry and processing conditions on additive manufacturability of Ni-based superalloys, in: S. Tin, C. O'Brien, J. Clews, J. Cormier, Q.C. Feng, M. Hardy, J. Marcin, A. Suzuki (Eds.), Superalloys 2020, The Minerals, Metals & Materials Series, Springer, 2020, pp. 153–162.

[38] D. Grange, J. Bartout, B. Macquaire, C. Colin, Processing a non-weldable nickel-base superalloy by selective laser melting: role of the shape and size of the melt pools on solidification cracking, Materialia 12 (2020) 100686.

[39] M. Dimter, R. Mayer, L. Hummeler, R. Salzberger, J. Kotila, T. Syvanen, Method and device for manufacturing a three-dimensional object, 2008.

[40] QUANTAXCrystAlign: Fully-integrated high-performance EBSD analysis system, Bruker Nano GmbH, Schwarzschildstrasse 12, 12489 Berlin.

[41] Oxford Instrument HKL Channel 5, Oxford Instruments HKL, Majsmarken 1, 9500 Hobro, Denmark.

[42] A.J. Wilkinson, D. Randman, Determination of elastic strain fields and geometrically necessary dislocation distributions near nanoindents using electron back scatter diffraction, Philos. Mag. 90 (9) (2010) 1159–1177.
[43] S. Sulzer, E. Alabort, A. Németh, B. Roebuck, R. Reed, On the rapid assessment of mechanical behavior of a prototype nickel-based superalloy using small-scale testing, Metall. Mater. Trans. A 49 (9) (2018) 4214–4235.
[44] S. Kou, Welding Metallurgy, 2nd ed., John Wiley & Sons, Inc., 2002.
[45] D. Dye, O. Hunziker, R. Reed, Numerical analysis of the weldability of superalloys, Acta Mater. 49 (4) (2001) 683–697.
[46] J.C. Lippold, Welding Metallurgy and Weldability, John Wiley & Sons, Inc., 2014.
[47] M.G. Collins, J.C. Lippold, An investigation of ductility dip cracking in nickel-based filler materials-part i, Weld J. (2003) 288–295.
[48] A. Ramirez, J. Lippold, High temperature behavior of Ni-base weld metal: part ii - insight into the mechanism for ductility dip cracking, Mater. Sci. Eng. A 380 (1) (2004) 245–258.
[49] Y. Tian, D. Tomus, P. Rometsch, X. Wu, Influences of processing parameters on surface roughness of hastelloy x produced by selective laser melting, Addit. Manuf. 13 (2017) 103–112.
[50] J. Jiang, T.B. Britton, A.J. Wilkinson, Accumulation of geometrically necessary dislocations near grain boundaries in deformed copper, Philos. Mag. Lett. 92 (11) (2012) 580–588.
[51] W. Boettinger, U. Kattner, K. Moon, J. Perepezko, DTA and Heat Flux DSC Measurements of Alloy Melting and Freezing, National Institute of Standards and Technology Special Publication, pp. 151–221.
[52] S. Kou, A criterion for cracking during solidification, Acta Mater. 88 (2015) 366–374.
[53] M. Rappaz, J.M. Drezet, M. Gremaud, A new hot-tearing criterion, Metall. Mater. Trans. A 30 (2) (1999) 449–455.
[54] M. Rappaz, A. Jacot, W.J. Boettinger, Last-stage solidification of alloys: theoretical model of dendrite-arm and grain coalescence, Metall. Mater. Trans. A 34 (3) (2003) 467–479.
[55] S. Griffiths, H. Tabasi, T. Ivas, X. Maeder, A. De Luca, K. Zweiacker, R. Wrobel, J. Jhabvala, R. Logé, C. Leinenbach, Combining alloy and process modification for micro-crack mitigation in an additively manufactured Ni-base superalloy, Addit. Manuf. (2020) 101443.
[56] Y.L. Tsai, S.F. Wang, H.Y. Bor, Y.F. Hsu, Effects of Zr addition on the microstructure and mechanical behavior of a fine-grained nickel-based superalloy at elevated temperatures, Mater. Sci. Eng. A 607 (2014) 294–301.
[57] Y. Zhao, J. Zhang, Y. Luo, B. Zhang, G. Sha, L. Li, D. Tang, Q. Feng, Improvement of grain boundary tolerance by minor additions of Hf and B in a second generation single crystal superalloy, Acta Mater. 176 (2019) 109–122.
[58] L. Yuan, C. O'Sullivan, C. Gourlay, Exploring dendrite coherency with the discrete element method, Acta Mater. 60 (3) (2012) 1334–1345.
[59] Q. Jia, P. Rometsch, P. Kürnsteiner, Q. Chao, A. Huang, M. Weyland, L. Bourgeois, X. Wu, Selective laser melting of a high strength AlMnSc alloy: alloy design and strengthening mechanisms, Acta Mater. 171 (2019) 108–118.
[60] H.C. Basoalto, C. Panwisawas, Y. Sovani, M.J. Anderson, R.P. Turner, B. Saunders, J.W. Brooks, A computational study on the three-dimensional printability of precipitate-strengthened nickel-based superalloys, P. Roy. Soc. A, vol. 474, Royal Society Publishing, 2018.
[61] P.A. Hooper, Melt pool temperature and cooling rates in laser powder bed fusion, Addit. Manuf. 22 (2018) 548–559.
[62] P. Kürnsteiner, M. Wilms, A. Weisheit, B. Gault, E. Jägle, D. Raabe, High-strength damascus steel by additive manufacturing, Nature 582 (2020) 515–519.
[63] M.J. Anderson, C. Panwisawas, Y. Sovani, R.P. Turner, J.W. Brooks, H.C. Basoalto, Mean-field modelling of the intermetallic precipitate phases during heat treatment and additive manufacture of Inconel 718, Acta Mater. 156 (2018) 432–445.
[64] A. Németh, D. Crudden, D. Armstrong, D. Collins, K. Li, A. Wilkinson, C. Grovenor, R. Reed, Environmentally-assisted grain boundary attack as a mechanism of embrittlement in a nickel-based superalloy, Acta Mater. 126 (2017) 361–371.
[65] L. Nastac, D.M. Stefanescu, Computational modeling of NbC/laves formation in INCONEL 718 equiaxed castings, Metall. Mater. Trans. A 28 (7) (1997) 1582–1587.
[66] A. Egbewande, H. Zhang, R. Sidhu, O. Ojo, Improvement in laser weldability of INCONEL 738 superalloy through microstructural modification, Metall. Mater. Trans. A 40 (11) (2009) 2694.
[67] Y.T. Tang, J.N. Ghoussoub, C. Panwisawas, D.M. Collins, S. Amirkhanlou, J.W. Clark, A.A. Németh, D.G. McCartney, R.C. Reed, The effect of heat treatment on tensile yielding response of the new superalloy ABD-900AM for additive manufacturing, in: S. Tin, C. O'Brien, J. Clews, J. Cormier, Q.C. Feng, M. Hardy, J. Marcin, A. Suzuki (Eds.), Superalloys 2020, The Minerals, Metals & Materials Series, Springer, 2020, pp. 1055–1065.
[68] P.M. Mignanelli, N.G. Jones, M.C. Hardy, H.J. Stone, On the time-temperature–transformation behavior of a new dual-superlattice nickel-based superalloy, Metall. Mater. Trans. A 49 (2018) 699–707.
[69] T.B. Gibbons, R. Stickler, IN939: Metallurgy, properties and performance, in: R. Brunetaud, D. Coutsouradis, T. Gibbons, Y. Lindblom, D. Meadowcroft, R. Stickler (Eds.), High Temperature Alloys for Gas Turbines 1982, 1982.
[70] J.R. Davis, ASM Specialty Handbook: Heat-Resistant Material, ASM International, 1997.
[71] O. Oguntuase, O.A. Ojo, J. Beddoes, Influence of post-deposition heat treatments on the microstructure and mechanical properties of wire-arc additively manufactured ATI 718Plus, Metall. Mater. Trans. A 51 (2020) 1846–1859.
[72] Y. Idell, L. Levine, A. Allen, F. Zhang, C. Campbell, G. Olson, J. Gong, D.R. Snyder, H.Z. Deutchman, Unexpected δ-phase formation in additive-manufactured ni-based superalloy, JOM 68 (2016) 950–959.
[73] E. Chlebus, K. Gruber, B. Kuźnicka, J. Kurzac, T. Kurzynowski, Effect of heat treatment on the microstructure and mechanical properties of Inconel 718 processed by selective laser melting, Mater. Sci. Eng. A 639 (2015) 647–655.
[74] D. Tomus, P.A. Rometsch, M. Heilmaier, X. Wu, Effect of minor alloying elements on crack-formation characteristics of Hastelloy-X manufactured by selective laser melting, Addit. Manuf. 16 (2017) 65–72.
[75] E.G. Thompson, S. Nunez, M. Prager, Practical solutions to strain age cracking in René 41, Weld. J. 47 (7) (1968) 299–313.
[76] M.B. Henderson, D. Arrell, R. Larsson, M. Heobel, G. Marchant, Nickel based superalloy welding practices for industrial gas turbine applications, Sci. Technol. Weld. Joi. 9 (1) (2004) 13–21.
[77] J. Robson, Modelling the evolution of particle size distribution during nucleation, growth and coarsening, Mater. Sci. Technol. 20 (4) (2004) 441–448.
[78] S. Meher, M. Carroll, T. Pollock, L. Carroll, Designing nickel base alloys for microstructural stability through low γ/γ' interfacial energy and lattice misfit, Mater. Des. 140 (2018) 249–256.
[79] K. Chen, J. Wu, H. Shi, X. Chen, Z. Shen, M. Zhang, L. Zhang, A. Shan, Transition of deformation behavior and its related microstructure evolution in Nimonic 80A under hot-to-warm working, Mater. Charact. 106 (2015) 175–184.